

# Ultrafast photo-ion probing of the relaxation dynamics in 2-thiouracil.

Matthew S. Robinson<sup>1,2,3\*</sup>, Mario Niebuhr<sup>1</sup> and Markus Gühr<sup>1,\*</sup>

<sup>1</sup> Universität Potsdam, Institut für Physik und Astronomie, Karl-Liebknecht-Straße 24/25, 14476 Potsdam-Golm, Germany

<sup>2</sup> Center for Free-Electron Laser Science (CFEL), Deutsches Elektronen Synchrotron (DESY), Notkestraße 85, 22607 Hamburg, Germany

<sup>3</sup> The Hamburg Centre for Ultrafast Imaging, Universität Hamburg, Luruper Chaussee 149, 22761 Hamburg, Germany

\* Correspondence: MSR: matthew.robinson@cfel.de, MG: mguehr@uni-potsdam.de

**Abstract:** In this work we investigate the relaxation processes of 2-thiouracil after UV photoexcitation to the  $S_2$  state through the use of ultrafast, single-color, pump-probe UV/UV spectroscopy. We place focus on investigating the appearance and subsequent decay signals of ionized fragments. We complement this with VUV-induced dissociative photoionization studies collected at a synchrotron, allowing us to better understand and assign the ionisation channels involved in the appearance of the fragments. We find that all fragments appear when single photons with energy  $> 11$  eV are used in the VUV experiments and hence appear through 3+ photon-order processes when 266 nm light is used the UV/UV experiment. We also observe three major decays for the fragment ions: a sub-autocorrelation decay (i.e. sub-370 fs), a secondary ultrafast decay on the order of 300-450 fs, and a long decay on the order of 220 to 400 ps (all fragment dependent). These decays agree well with the previously established  $S_2 \rightarrow S_1 \rightarrow \text{Triplet} \rightarrow \text{Ground}$  decay process. Results from the VUV study also suggest that some of the fragments may be created by dynamics occurring on the excited cationic state.

**Keywords:** thiouracil; uracil; pump-probe spectroscopy; ultrafast mass spectroscopy; PEPICO; ultrafast dynamics; ultrafast relaxation processes.

## 1. Introduction

Despite readily absorbing UV light, DNA and RNA nucleobases have the ability to undergo rapid relaxations through singlet and triplet manifolds to dissipate electronic energy into vibrational states [1–7]. This relaxation determines the remarkable photostability of the nucleobases and, in addition, is thought to be one of the important mechanisms contributing to the photostability of the genetic code by reducing the occurrence of UV-induced lesions [7–12].

Among the important UV-induced damages in nucleic acids, the cyclopyrimidine dimer (CPD) occurring among neighbouring thymine bases is the most abundant [13], and thus the UV-induced relaxation in thymine, as well as other nucleobases such as uracil, has been studied extensively [7,10,14,15]. However, naturally occurring variants of canonical nucleobases, like the commonly-studied thionated nucleobases, where one or more of the oxygen atoms is substituted for a sulfur atom, can appear with their own unique chemical features. The most striking of these is the efficient creation of long-lived triplet states [16–18], which pose a risk to live tissue due to the creation of reactive singlet oxygen as well as initiating interstrand crosslinking in DNA [9,19–22]. The suspected origin of this feature among thionucleobases is attributed to a lowering of the triplet excited state minima with respect to its conical intersections with the ground state. This barrier shift changes the likelihood that certain relaxation pathways will be explored compared to its canonical counterpart [23]. Already, a number of ultrafast relaxation studies of thionated nucleobases have been performed, providing us with opportunities to better understand the decay mechanisms of canonical and thionated nucleobases alike. [14,16,17].

One of the most studied thionucleobases is 2-thiouracil (2TU) [16,23–26]. For 2TU, both quantum calculations [26–28] and ultrafast experiments [2,24,29,30] indicate it will generally be excited by UV light to the  $S_2$  state (peaking at 4.2 eV /295 nm,  $^1\pi_s\pi_s^*$  in the orbital naming conventions suggested by Mai *et al.* [27]). A rapid internal conversion from the photoexcited  $S_2$  to the optically dark  $S_1(^1n_s\pi_s^*)$  states is generally established as a doorway mechanism to lower triplet states. Pollum and Crespo-Hernández investigated the molecular dynamics in solution and reported a sub-200 fs decay for the  $S_2 \rightarrow S_1$  internal conversion [30], whilst computational work by Mai *et al.* [23,26,27], along with gas-phase experimental work by the Ullrich group [24,29,31,32] attribute a sub-100 fs decay to the internal conversion. After

relaxation to the  $S_1$  state, intersystem crossing to the triplet manifold occurs after some hundred femtoseconds. In solution phase, this process is attributed to an experimentally observed decay of 300-400 fs after a 316 nm excitation [30]. In gas phase, the time constant is found to vary between 200 and 775 fs with increasing excitation wavelength between 207 and 292 nm [31]. The molecule remains in these states for several ten to hundred picoseconds depending on the excitation wavelength [2,24,29,31]. Ultrafast x-ray Auger probing performed in our group allowed us to confirm the initial elongation of the C-S bond upon photoexcitation [33]. In addition, we performed ultrafast x-ray photoelectron spectroscopy on UV-excited 2TU, generally confirming the established pathways, but finding that part of the photoexcited population relaxes immediately into the ground state within 250 fs, as well as noting coherent 250 fs oscillations stemming from modulated population exchange between the  $S_1$  state and other states [34].

In this work, we look to further our understanding of the ultrafast dynamics of 2TU through lab-obtained UV/UV pump-probe photo-ion studies. Similar work by Ghafur *et al.* has been performed in the past [2], which successfully elucidated excited-state dynamics of 2TU. The work presented here advances the idea through unique comparisons to complementary vacuum ultraviolet (VUV) dissociative photoionization data obtained at a synchrotron. These novel comparisons allow us to obtain an overall deeper understanding about the likely origins of each fragment ion, and how these appearances depend on the UV-induced dynamics in the pump-probe spectroscopy. These results help shape our picture of 2TU in terms of potential energy surfaces and molecular geometry changes in the relaxation process.

The remainder of this article is as follows: In Section 2 we present results, split into several subsections, detailing results from different UV/UV and VUV experiments. In Section 3, we interpret these results, discussing how they reflect on previously published work and improve our understanding of the relaxation processes of 2TU. In Section 4, we describe the experimental set-up and parameters used in both the ultrafast UV/UV ion fragmentation studies and the VUV studies performed at the Swiss Light Source (SLS). Finally, in Section 5 we present our conclusions.

## 2. Results

In this section we present results from both the VUV and UV/UV experiments. We start by detailing what fragment ions are observed in both experiments (Subsection 2.1.). This is then followed by results from the VUV work (Subsection 2.2.) and UV/UV experiments (Subsection 2.3. - 2.5.), respectively. With respect to the Subsections that concentrate on the UV/UV experiments, whilst a general description of the set-up can be found in Subsection 4.1, we briefly provide at the start of these Subsections the unique experimental parameters that are important to each of the UV/UV experiments discussed to help provide context to the reader.

### 2.1. Observed Fragments

We start with a brief summary of the highest abundance fragments observed after the photoionization of 2TU. An example from the UV/UV study can be seen in Figure 1, however, we mostly observe the same fragments in both the VUV and UV/UV experiments. Masses observed in both experiments include the 28, 41, 42, 58, 60, 69, 70, 95, 100 atomic mass unit (amu) fragment ions as well as the parent (128 amu) ion. These appearances agree well with photoionization mass spectra presented in past experiments [2,29,35,36]. Despite being observed, we will not discuss further the 58 and 60 amu fragments, as their signals were significantly weaker than other fragments. We will also not explicitly discuss the 70 amu fragment, as this always appeared as shoulder to the 69 amu fragment ion signal, and has been previously suggested to be the same fragment as the 69, albeit with an additional hydrogen atom attached [37]. We note that only a weak signal was observed for the 96 amu fragment in the VUV studies to be presented below, and not at all in the UV/UV studies (most likely due to signal strength), and therefore discussion on this fragment will be limited. Similarly, due to its weak signal strength, discussion of the time-dependent features of the 100 amu ion is not possible, however, its appearance in the first place is interesting in the context of past uracil studies [1,2,38], and so a discussion based on this can be found in the Supplementary Data.

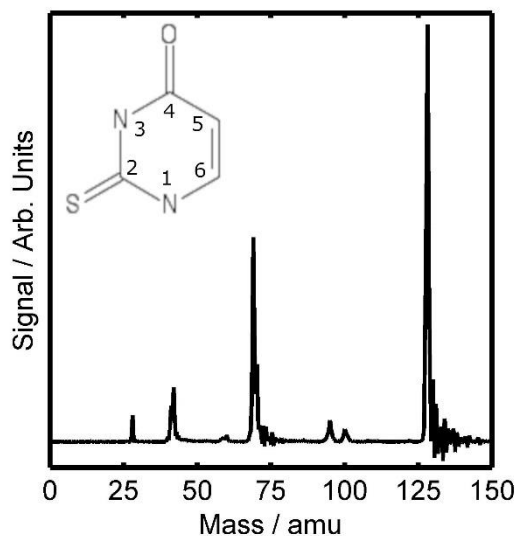


**Figure 1.** Typical photo-ion mass spectrum of 2TU taken from the UV/UV experiment. Data was recorded at the pump-probe temporal overlap, with a combined pump-probe energy of 13 nJ. The insert shows the numbered 2TU molecule. As we do not have indications of fragment charges higher than one, the x-axis gives the ion mass.

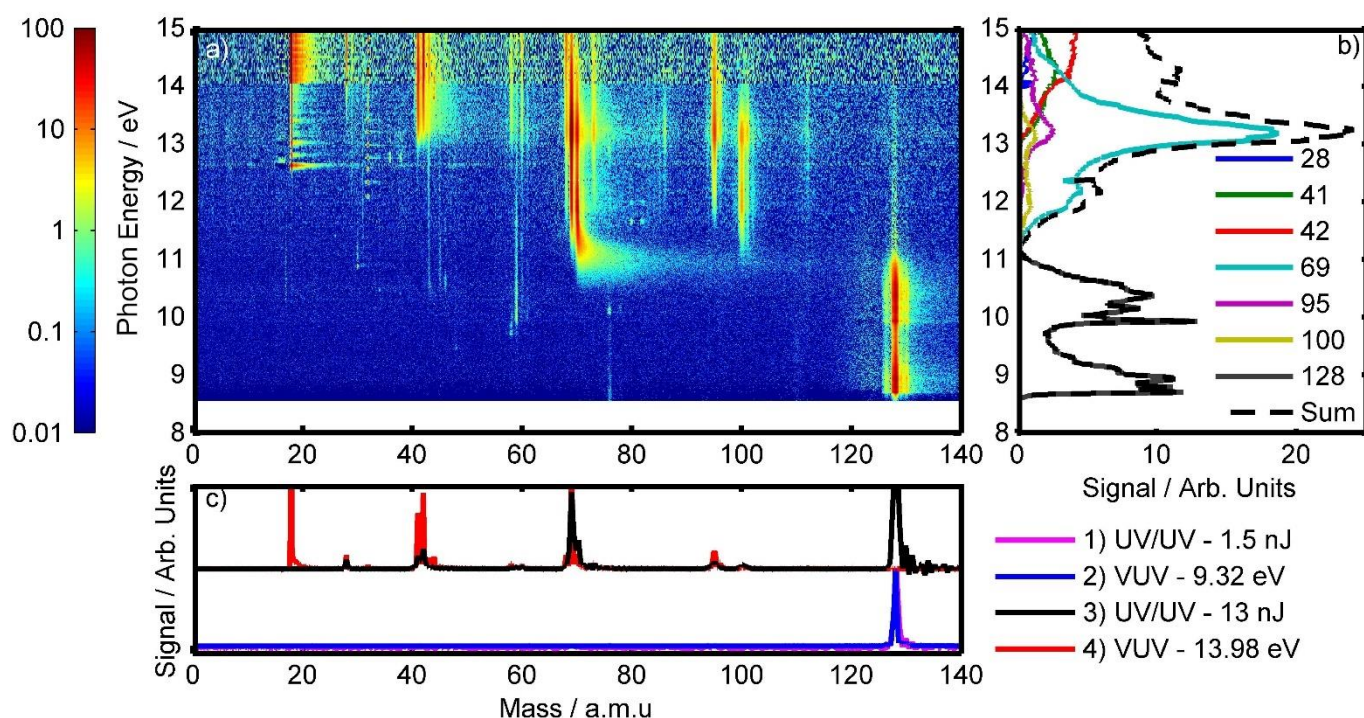


**Figure 2.** a) Logarithmic false-color representation of the background-corrected VUV data collected at SLS showing threshold-ionization-selected ions collected *via* the PEPICO method for photon energies between 8.55 and 15 eV. b) ms-TPES for select fragments. c) Cuts of the VUV data along the mass axis at energies that correspond to 2-photon (9.32 eV) and 3-photon (13.98 eV) ionization at 266 nm, overlain with low- and high-power signals from the UV/UV experiment, respectively, obtained at time-zero.

## 2.2. VUV (PEPICO) Studies

Figure 2 presents data from the VUV photoelectron-photoion coincidence (PEPICO) experiment performed at SLS. Data were collected using photons with energy ( $h\nu$ ) in the range of  $h\nu = 8.55$ -15 eV, and is stitched together from three runs (see Section 4.2 for full details). As the main focus of this paper is the UV/UV experiment, only a coarse analysis of the VUV data will be made here to assist this work. Figure 2a shows a false-color plot, on a logarithmic scale, detailing which mass fragments are observed

in coincidence to the arrival of near-zero kinetic energy electrons at our detector for specific VUV photons.

Figure 2b shows the mass-specific lineouts taken from Figure 2a, which give the mass-selected threshold photoelectron spectra (ms-TPES) [39]. These show how the fragment-specific signals vary with respect to the VUV photon energy used. Whilst it is possible to draw analogies between an ms-TPES and photoelectron spectra, it is important to note that the two methods provide different information. Photoelectron spectra generally represent a full kinetic energy range, whilst ms-TPES is based on low energy electrons (up to *ca.* 10 meV) coincident with the respective ion. The ms-TPES is useful for the identification of ionization thresholds with new cationic states, and how these states cause different fragmentation events.

**Table 1.** Attribution of the fragment ions of 2TU to chemical formulae, along with the respective appearance energies observed in the VUV photofragmentation studies, fitted using the Asher model [40]. Comparisons are also made to similar fragments observed in the uracil work of Jochims *et al.* [37].

Mass/ amu	Attributed Formula	Appearance Energies / eV	Appearance energy in uracil / eV[37]
28	HCNH <sup>+</sup>	14.04 ± 0.02	13.75 ± 0.05
41	C <sub>2</sub> NH <sub>3</sub> <sup>+</sup>	13.47 ± 0.01	12.95 ± 0.05
42	C <sub>2</sub> H <sub>2</sub> O <sup>+</sup>	13.83 ± 0.01	13.25 ± 0.05
69	C <sub>3</sub> NH <sub>3</sub> O <sup>+</sup>	11.90 ± 0.01	10.95 ± 0.05
95	C <sub>4</sub> N <sub>2</sub> H <sub>3</sub> O <sup>+</sup>	12.65 ± 0.02	Observed, but not given
96	C <sub>4</sub> N <sub>2</sub> H <sub>4</sub> O <sup>+</sup>	13.59 ± 0.01	Observed, but not given
100	C <sub>3</sub> N <sub>2</sub> H <sub>4</sub> S <sup>+</sup>	11.95 ± 0.01	Not observed
128 (Parent)	C <sub>4</sub> N <sub>2</sub> H <sub>4</sub> SO <sup>+</sup>	8.73 ± 0.002	9.15 ± 0.03

In Table 1, we present the appearance energies of the ions of interest, fitted using the Asher model [40]. Whilst alternative fitting models that take into account a wider range of parameters for more accurate models are available (e.g. Rice–Ramsperger–Kassel–Marcus (RRKM) theory and Simplified Statistical Adiabatic Channel Model (SSACM) [41,42]) only approximate energies are needed to support the UV/UV work presented here, and hence the Asher model suffices.

### 2.3. UV/UV Power Series

Here, we discuss a power series scan performed using the UV/UV set-up to determine the photon-dependency for each of the fragments of interest. This experiment is similar to the power-dependency studies of rare gases performed by L’Huillier *et al.* [43]. The scans were performed over a range of pump-probe delays, allowing us to identify time-dependent changes in the observed photon-dependencies (similar to work performed by Koch *et al.* [44]). Mass spectra were collected for a set of pump-probe pulse energies; a total of between 1.6 and 19.7 nJ was split evenly between the two beams, over pump-probe delays of 0, 0.1, 0.5, 1, 5, and 10 ps.

For each data point collected, the area under each mass peak of interest was integrated (referred to as the “Signal” from here on) and plotted against the combined pump-probe energy as a function of  $\text{Log}_{10}(\text{Signal})$  Vs  $\text{Log}_{10}(\text{Laser Energy})$ . A selection of prominent mass peaks can be seen in **Figure 3**, whilst full plots for all ions of interest can be found in Figures S1-6 in the Supplementary Data. In the region where the signal was both above background and not saturating, the plots were fitted to a straight line to obtain a gradient; specifically, the parent ion, 69 amu fragment ion and the remaining fragment ions of interest were fitted in the ranges of 1.6 – 9.3 nJ, 3.6 – 13.7 nJ, and 9.3 - 19.7 nJ, respectively. The values of the fitted gradients provide a strong indication to the number of photons needed to create the each ion [43,44]. A summary of the fragment- and delay-dependent gradients can be found in **Table 1**.

As Table 2 details, the value of the fitted gradient for the parent ion is relatively constant at all pump-probe delays, with an average value of  $1.9 \pm 0.1$ . This is a strong indication that the parent ion is produced through a two-photon process when using 266 nm photons.

**Table 2.** Fitted slopes values for  $\text{Log}_{10}(\text{Signal})$  Vs  $\text{Log}_{10}(\text{Laser Energy})$  plots for the fragments of interest observed in the UV/UV experiment at various pump-probe delay times.

Delay (ps)	28 amu	41 amu	42 amu	69 amu	95 amu	Parent
0.0	$2.94 \pm 0.54$	$2.68 \pm 0.15$	$2.72 \pm 0.14$	$2.50 \pm 0.34$	$2.56 \pm 0.2$	$1.87 \pm 0.06$
0.1	$3.94 \pm 0.29$	$2.87 \pm 0.06$	$2.90 \pm 0.10$	$2.64 \pm 0.05$	$2.74 \pm 0.09$	$1.86 \pm 0.04$
0.5	$3.45 \pm 0.70$	$2.76 \pm 0.16$	$2.85 \pm 0.20$	$2.81 \pm 0.44$	$2.48 \pm 0.12$	$1.75 \pm 0.11$
1	$3.18 \pm 1.24$	$2.76 \pm 0.37$	$2.77 \pm 0.33$	$2.70 \pm 0.15$	$2.69 \pm 0.53$	$1.75 \pm 0.05$
5	$3.58 \pm 0.30$	$2.90 \pm 0.08$	$2.91 \pm 0.10$	$2.71 \pm 0.10$	$2.80 \pm 0.16$	$1.99 \pm 0.06$
10	$3.58 \pm 0.27$	$2.90 \pm 0.23$	$2.95 \pm 0.05$	$2.71 \pm 0.05$	$2.69 \pm 0.30$	$1.86 \pm 0.03$

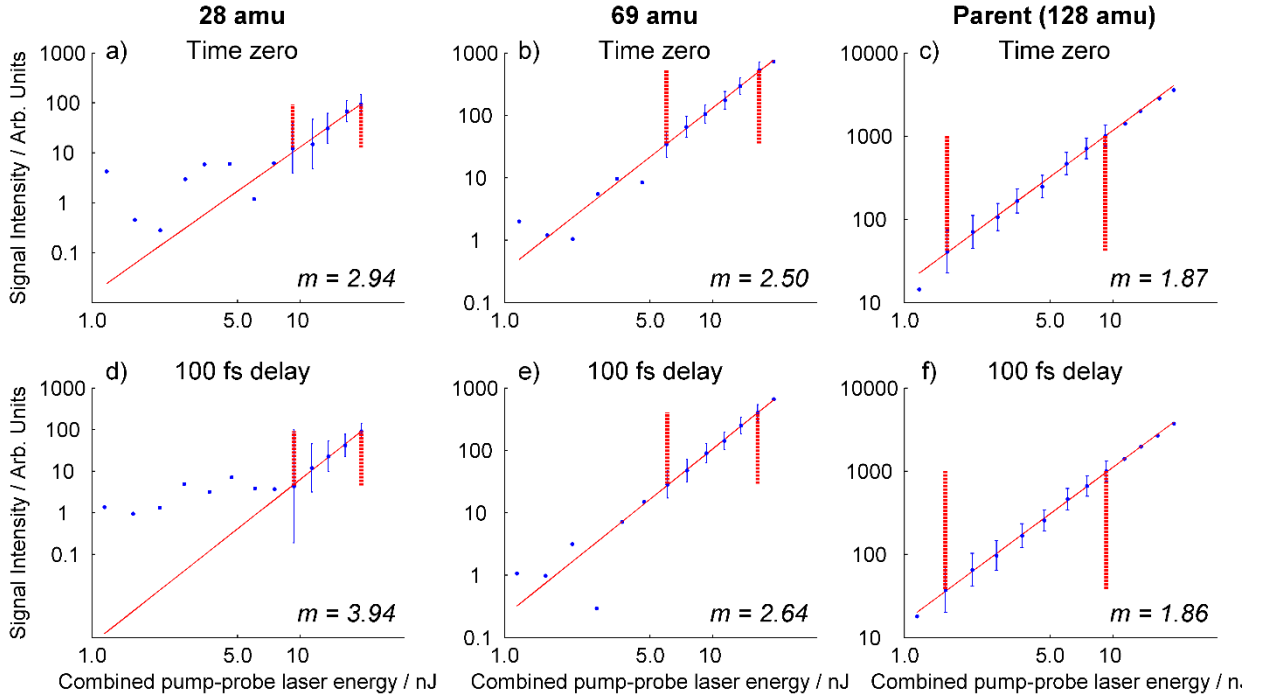


**Figure 3.** Power series plots (displayed in a “log-log” format) showing how the Signal varies with respect to the combined pump-probe laser energy for the 28 amu fragment ion (parts a and d), the 69 amu fragment ion (parts b and e), and the parent (128 amu) ion (parts c and f) for the time-zero overlap (parts a, b and c) and a 100 fs pump-probe delay (parts d, e and f). The dotted red lines show the region in which the slope of  $\text{log}_{10}(\text{Signal})$  Vs  $\text{log}_{10}(\text{Laser Energy})$  was fitted for each fragment. The resulting fit is shown by the solid red line. The value of the fitted gradient,  $m$ , is shown in the bottom right corner of each plot, its measurement uncertainties are given in Table 2. Error bars outside of the fitting region have been excluded due to their unreliability caused by either a limited or saturated signal.

All of the fragment ions have slope values that are higher than 2, suggesting higher-order processes. In particular, values of the slopes for the 41, 42, 69, and 95 amu fragments all lie between 2.5 and 3 for all time delays measured, suggesting that three photons of 266 nm light are needed to produce these fragments. For the 28 amu fragment, we observe a slope of 2.9 at time zero, which then increases to between 3.2 and 3.9 for all other delays. This suggests a change in photon-order from 3→4 as one moves away from the pump-probe temporal overlap.

#### 2.4. Time-dependent UV/UV signal from pump-probe beams with equal power

The time-dependent photo-ion signals for the masses of interest when using UV/UV pump and probe beams of equal powers was collected over three experiments. The first was a “low-power” scan, using a combined (i.e. incoherently summed) pulse energy of  $(7.4 \pm 0.1)$  nJ, over a delay range of  $-1 \rightarrow 1$  ps; this allowed for a non-saturated parent ion signal to be collected. The second experiment was a “high-power” scan, using a combined pulse energy of  $19.7 \pm 0.1$  nJ, over a delay range of  $-3 \rightarrow 15$  ps;

this allowed for time-dependent data of the fragment ions around time zero region to be acquired. The third experiment was also a “high power” experiment (i.e. same laser settings), scanned over the range of  $0 \rightarrow 100$  ps; this allowed for the longer decay processes of the fragments to be studied.

**Figure 4** shows the time-dependent signals of the 28 amu (a), 69 amu (b) and parent ions (c). Plots for other ions can be found in the supplementary data in Figures S7-S9. For all ions, a “fast” signal drop within the first picosecond around the time-zero position was observed. After this, the parent ion signal simply decayed to the background level. Most fragment ions show slow decays that remained above the background level for hundreds of picoseconds. Subplots have been included in **Figure 4a** and **b** to show the longer-lived decays for the 28 and 69 amu ions, respectively.

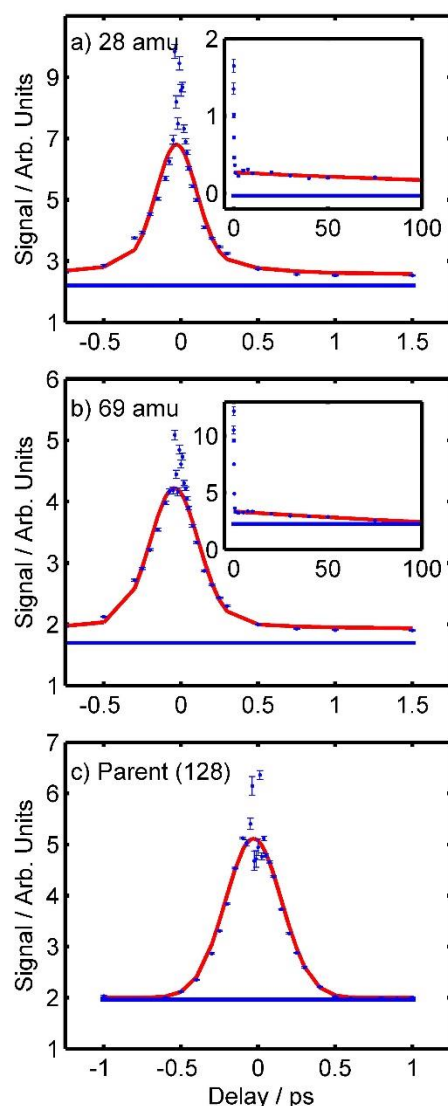


**Figure 4.** Time-resolved signals for the a) 28 amu b) 69 amu and c) Parent (128 amu) ions. The original data is represented by the blue dots, the fit of this data by the red line, and the background signal by the blue line. In a) and b) inserts show the respective signal for the fragment ions extending out to 100 ps.

Fits of the data seen in Figure 4 were performed to determine the decay constants of the individual ions. These fits exclude the coherent artefact seen around the time-zero delay for a number of the ions, which likely arises due to under-sampling an ultrafast decay whose lifetime is shorter than our auto-correlation signal. Assignment of these ultrafast decays will be discussed in due course of this paper, yet more information on the origin of this artefact can be seen in our previous publication [45]. The parent ion was initially fit to a Gaussian curve with a FWHM that matched the FWHM of the two-photon 1,4-dioxane ionization signal observed in the auto-correlation experiment described in Subsection 4.1, convoluted with a single decaying exponential with a decay constant of  $\tau_1$ . However,  $\tau_1$  simply

tended to zero in the fitting process. This suggests that the shape of the parent ion signal closely matches the FWHM of the autocorrelation experiment.

For the 41, 42, 69 and 95 amu fragments, fitting of the data was performed in two parts. First, to obtain a measure of the slow decay, a simple exponential decay function, with decay constant  $\tau_3$ , was fit to the data in the range of 1 to 100 ps. Next, fits of the data in the range of -3 to 15 ps were performed, using a Gaussian, whose FWHM matched the FWHM of the three-photon xenon signal collected in the auto-correlation experiments described in Subsection 4.1, convoluted with three decaying exponentials. During the fitting routine, the amplitudes and decay constants of two of the decaying exponentials,  $\tau_1$  and  $\tau_2$  were allowed to refine freely (after an appropriate initial estimate). The decay constant of the third exponential was fixed to previously determined  $\tau_3$  value, whilst its amplitude was allowed to refine freely. For all fragments, both the time-zero position and the FWHM of the Gaussian were refined for best fit, however, it was found that the FWHM never changed by more than a few femtoseconds from the values predicted by the auto-correlation experiments.

In performing the fits for the 41, 42, 69 and 95 amu fragments, it was found that the value of  $\tau_1$  tended to zero, suggesting that the data around time zero was primarily the same as the auto-correlation signal. For the 41, 69 and 95 amu fragment ions it was possible to refine a unique value for  $\tau_2$ . In the case of the 42 amu fragment ion, the  $\tau_2$  value either tended to the same near-zero value of  $\tau_1$ , or its amplitude tended to zero, suggesting that no unique  $\tau_2$  value could be fit.

The fitting of the 28 amu fragment ion generally followed a similar procedure as with the other fragment ions. However, due to the four-photon dependency of the 28 amu fragment ion outside of the time-zero position, it was decided that a 300 fs FWHM Gaussian should be used to represent the auto-correlation in the convolution to fit the data, better matching the expected duration of a four-photon auto-correlation signal of our set-up. A summary of the fitted decay constants can be found in **Table 3**.

**Table 3.** Fitted decay constants for the parent and fragments of 2TU as observed in the UV/UV time-resolved experiment

Ion	$\tau_1$ / fs	$\tau_2$ / fs	$\tau_3$ / ps
Parent		N/A	N/A
28		$330 \pm 156$	$218 \pm 60$
41	Tends	$398 \pm 270$	$343 \pm 61$
42	to zero	N/A	$301 \pm 46$
69		$417 \pm 321$	$309 \pm 25$
95		$340 \pm 127$	$380 \pm 160$

### 2.5. Time-dependent UV/UV signals from pump and probe beam with unequal powers

In these experiments, variable ND filters were inserted into the Michelson Interferometer, allowing for unequal pump and probe powers. The probe beam was fixed to a pulse energy of 3 nJ, whilst the pump beam was scanned over a set of pre-selected pulse energies of 1.5, 3, 6 and 9 nJ. The insertion of these ND filters into the beam line caused the pump-probe temporal overlap to be shifted slightly from that used in Subsections 2.3. and 2.4. due slight differences in the thickness of the ND filters (inherent in their manufacturing). Time-dependent scans were performed over the region  $\pm 1.5$  ps around the time-zero position located in the previous experiments, and the data presented here has been adjusted so as to place the time-zero position the point of most intense signal.

Figure 5 shows the time-dependent signals for the parent and 69 amu fragment ion using pump and probe beams of unequal power. Plots relating to the other fragment ions are presented in Figures S10-S13 of the Supplementary Data. In this figure, we plot both the pump-probe data (i.e. positive delay times where the pump beam arrives first) and the probe-pump data (i.e. negative delay times where the pump beam arrives second) in the positive x-axis direction. This allows for a direct comparison between the pump-probe and probe-pump signals.

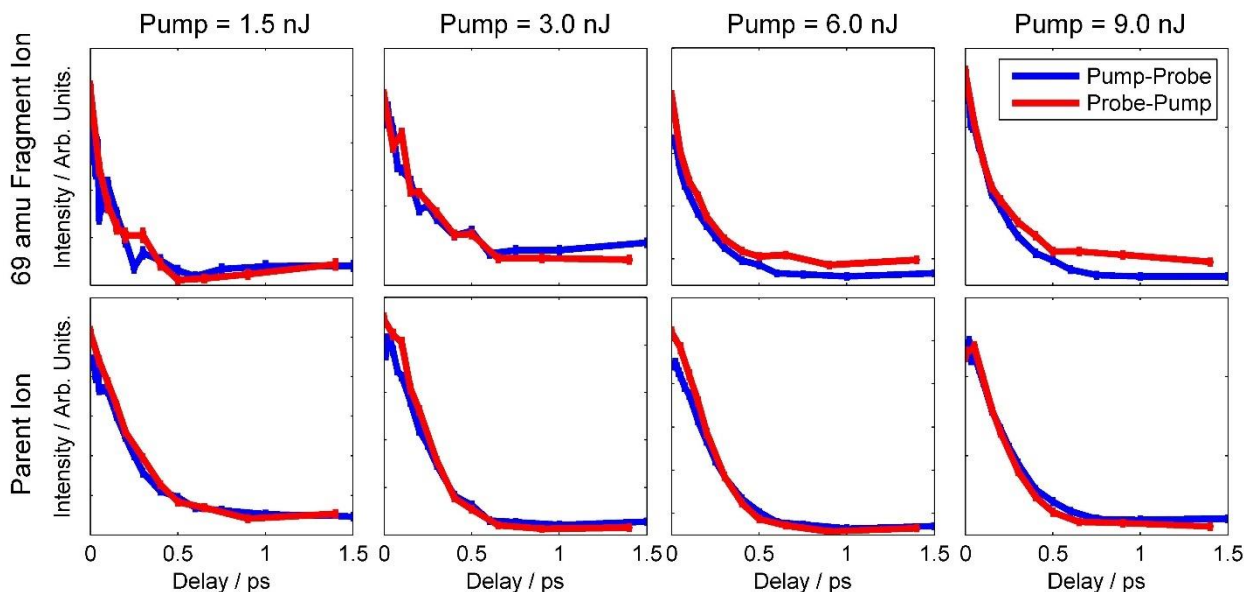


**Figure 5.** Time-dependent signals observed for the 69 amu fragment ion (Top) and the parent (128 amu) ion (Bottom) when unequal pump and probe powers are used. The measurement values are given by the symbols, where the uncertainty interval is given by its height, with lines connecting the symbols. Signals from a range of pump pulse energies were used (from left to right: 1.5, 3, 6 and 9 nJ) in conjunction with the probe pulse, which was fixed at 3 nJ. In each image, two plots are shown which dictate whether the pump pulse arrives first (pump-probe, blue) or if the probe pulse arrives first (probe-pump, red).

Concentrating first on the parent ion, we can see that the both the pump-probe and probe-pump plots are very similar to one another, showing similar decay rates and similar baseline levels at longer decays (i.e. 500+ fs). The signal of the 69 amu fragment ion, however, does not show this degeneracy. In the case where the pump beam is either the same as, or weaker than, the probe beam (i.e. pump  $\leq$  3.0 nJ), the pump-probe and probe-pump plots show similar time-dependent features. However, when the pump beam is stronger than the probe beam (i.e. pump  $>$  3.0 nJ), an offset between the two plots is observed, most notable at longer delay times (i.e. 500+ fs). One can see that when using these higher pump powers, the probe-pump signal is stronger than that of the pump-probe signal.

For the remaining fragments ions, a signal above background is only observed when the pump pulse energy was 6 nJ or above, in addition to the 3 nJ probe pulse. This is in line with what was noted in Subsection 2.3., where a signal above background was only observed when the combined energy of the pump and probe pulses was  $\sim$ 9 nJ. Nonetheless, no significant difference between the pump-probe and probe-pump signals was observed for these fragments in these experiments.

### 3. Discussion

In this section, we will first provide an analysis of the VUV PEPICO results alongside the results from the UV/UV Power Series. This will allow us to obtain a general understanding at which VUV photon energies and UV photon orders (at 266 nm) certain ions appear. After this, we will dedicate a section to attributing the fragment ions to their respective chemical formulae, discussing what these fragments mean for the interpretation of 2TU dissociation and how the results compare to past studies. Finally, we will take an in-depth look at the VUV and UV/UV data for each ion, and its role in the interpretation of the ultrafast relaxation dynamics of 2TU.

#### 3.1. General analysis of VUV PEPICO results and UV/UV Power Series

A number of similarities can be seen between the “Summed” ms-TPES plot from the VUV PEPICO data seen in Figure 2b and the previously published photo-electron spectra of 2TU from Katritzky *et al.* [46]. The most notable of these are the two distinct bands centred around  $h\nu = 9$  and 10.5 eV. According to theoretical work by Ruckebauer *et al.* [25], the  $h\nu = 9$  eV band arises due to ionization of the n and  $\pi$



orbitals of the sulphur atom, whilst the  $h\nu = 10.5$  eV band originates from the ionization of the  $n$  and  $\pi$  orbitals of the oxygen atom [25].

For ionization energies of  $h\nu \geq 11.0$  eV, we see that the ms-TPES of the parent ion tends to zero and the fragment ions start to appear. At the same time, the “Summed” ms-TPES signal no longer corresponds as well with photo-electron spectra presented by Katritzky *et al.* [46] This is likely due to our spectrum being a threshold-electron correlated ion spectrum. The “summed” ms-TPES signal is only representative of the select masses of interest and not of all possible fragments.

The appearance of fragments at these higher photon energies suggest that the ejected electrons are critical to the bonding structure of the pyrimidine ring. From Table 1, one can note that all of the common fragment ions that appear for both 2TU and uracil have a higher appearance energy when originating from 2TU; this is despite 2TU having a lower ionization energy than uracil (8.73 Vs 9.15 eV) [37]. This may be an indication that the pyrimidine ring is more stable for 2TU, possibly due to the lower electronegativity of the sulfur atom allowing for more electron density to be distributed over the ring. In addition, the appearance of these fragments at these energies is in good agreement with theoretical work of Ruckebauer *et al.* which predicted that ionization of orbitals located on the pyrimidine ring would begin slightly above 11 eV [25]. In the same theoretical work, a strong ionization peak between 12-13 eV is predicted, and is attributed to the  $D_4$  ionization state. This prediction bares resemblance to the large peak seen at  $\sim 13$  eV in the summed ms-TPES data, with the 69 amu fragment ion being the main contributor to this peak. It is therefore possible that the  $D_4$  ionization primarily leads to the production of the 69 amu fragment ion.

Focusing on the UV/UV power series of Subsection 2.3., we saw that the parent ion was most likely created through a two-photon process when using 266 nm light. This photon order will supply  $\sim 9.32$  eV to the system, which agrees well with the VUV data, as it falls within  $\sim 8.5$ -11 eV appearance window for the parent ion. This also suggests that the parent ion signal observed in the UV/UV study is due to ionization of the  $n$  and  $\pi$  orbitals located at the sulfur atom of 2TU [25]. With respect to the fragment ions, we determined that these were all likely created through a three-photon order process or higher ( $h\nu \geq 13.98$  eV). This again agrees well with the VUV data, as fragments would only appear at energies above 11 eV, and hence a two-photon process is not sufficient.

With these results in mind, one would expect that if one was to use a “low” laser power in the UV/UV experiments, where there are enough photons present for a two-photon order process but high orders are negligible, one would only observe the parent ion. In the lower half of Figure 2c, we present a mass spectrum collected in one of these such “low-power UV/UV” experiments (pink line; 1.5 nJ used between the pump and probe pulses, overlapped at time zero), in which one can see that only the parent ion is observed. In the same plot, we directly compare this to the mass spectra observed in the VUV experiment using photons with an energy of  $9.32 \pm 0.1$  eV (i.e. two photons of 266 nm light, blue line). Once again, only the parent ion is observed, and two spectra are very similar, despite two different techniques being used.

Similarly, in the upper half of Figure 2c we compare a high-power UV/UV experiment (black, 13 nJ between the pump and probe pulses, overlapped at time zero) to a mass spectrum from the VUV for photons with energies of  $13.98 \pm 0.1$  eV (red, equivalent to three photons of 266 nm light). In these spectra, we can now see a multitude of fragments have appeared, including signals at 18 and 32 amu, which appear only in the VUV spectrum. These additional peaks most likely come from trace amounts of water vapour (mass = 18 amu, ionization energy = 12.6 eV [47]) and oxygen gas (mass = 32 amu, ionization energy = 12.1 eV [48]). Despite these contaminations, the remaining peak positions between the two spectra line up well with one another, further indicating that similar fragment ions are produced when a similar amount of energy is deposited into the system.

Whilst similar fragments are observed in both experiments, differences in the intensities of the ion peaks are apparent, likely due to the differences in the selectivity rules between the two experiments for observing ions. As noted previously, ions in the VUV PEPICO experiment are selectively observed in coincidence with near zero-energy threshold electrons, whilst in the UV/UV experiments no such selectivity is present. This is most exemplified by the parent ion, which appears as an oversaturated signal in the high-power UV/UV experiment, but not at all in the VUV experiment for 13.98 eV photons. The ms-TPES plot seen in Figure 2b shows that the parent ion only appears for photons in the  $\sim 8.5$ -11 eV range, while no threshold photoelectrons are connected to the parent ion at higher photon energies.

However, higher electron kinetic energies, not included in the measurement, might very well be correlated to the parent ion. For the UV/UV experiments, the inhomogeneity of the laser focus plays an important role for the observation of the parent. The inner part of the beam is intense and favours three-photon (or higher) processes leading to reduced parent intensity due to reduced dipole matrix elements. The outer part of the beam is of lower intensity and is therefore more suited for inducing lower-photon processes. As the outer area of the beam is larger than the inner area, this leads to a significant parent ion signal still being observed.

### 3.2. Fragment assignment and discussion of appearance.

The assignment of the major fragments observed in this work has been achieved through comparisons to past dissociation studies on uracil [1,2,35,37,38,49–54], as well as studies of 2TU [2,35,36,55]. A summary of the assignments has been included in **Error! Reference source not found.** As a formality for this section, we attribute the 128 amu ion to the parent ion,  $C_4N_2H_4SO^+$ .

We attribute the appearance of the 96 amu fragment to the direct loss of the sulfur atom (i.e.  $128 - 32 = 96$  amu), whilst the 95 amu fragment is most likely due to the combined loss of the sulfur atom and an additional hydrogen atom (i.e.  $128 - 32 - 1 = 95$  amu). Uleanya *et al.* also attributed the loss of the sulfur atom to a similar mass fragment in their protonated 2TU studies [36]. Additionally, equivalent ions have been observed in uracil experiments after a loss of oxygen (and hydrogen) [37,52]. We therefore attribute the 96 and 95 amu fragment ions of 2TU to the  $C_4N_2H_4O^+$  and  $C_4N_2H_3O^+$ , respectively.

Whilst for uracil it is difficult to determine if the  $C_2=O$  or  $C_4=O$  bond is broken to produce the 95/96 amu fragment ion [37], no such problem exists for 2TU due to the quasi-isotopic nature between the O and the S atoms. It is clear that the 96 amu fragment ion (and most likely the 95 amu fragment ion) appear due to the breaking of the  $C_2=S$  bond in 2TU [36]. Curiously, in the electron impact studies of the thiouracils by Hecht *et al.* [35], no peak was observed at 112 amu for 4-thiouracil, which would have indicated a  $C_2=O$  break. Instead, a peak at 95 amu was once again observed, indicating a loss of the sulfur (and hydrogen) from 4-thiouracil. This suggests that the ejection of this unit is more dependent on what type of atoms are attached to the pyrimidine ring, rather than where the atoms are positioned on the ring.

Generally, when the difference between fragments is a single hydrogen atom, the lighter mass has a higher appearance energy [37,38,56]. The fact that the 95 amu fragment ion of 2TU shows a lower appearance energy than the 96 amu ion may therefore suggest that there are novel processes involved in the ejection of the S and H atoms to create the 95 amu. Large vibrational/bending angles in the molecule which bring the sulfur and hydrogen atoms closer together could be one option [39]. Additionally, a migration of one of the atoms on a cationic state before the pair are ejected could be another option [57]. Interestingly, in the photochemistry studies of protonated 2TU by Uleanya *et al.*, where the extra proton sits on the sulfur atom, it was observed that a loss of both the sulfur and hydrogen atoms lead to their most abundant fragment ion signal (their  $96 \text{ amu} = 128 + 1 - (28 + 1)$ ) [36]. With reference to previous studies from Giuliani *et al.* [58] we are certain that at temperatures employed in our experiment, only the oxo-form of 2TU will appear and hence no tautomers with hydrogen directly bonded to sulfur are present in our studies, furthering the idea that dynamics after ionization may be at play.

The ejection of the stable (H)NCO fragment is commonly observed in canonical nucleobases [37,49,50,52,54,59,60], and in the case of uracil it leaves behind a 69 amu fragment ion, which is almost universally attributed to  $C_3NH_3O^+$  [35,37,38,49–52,54]. It is thought that the ejection of (H)NCO occurs through the breaking of the  $N_1C_2$  and  $N_3C_4$  bonds of the pyrimidine ring [54]. Like other studies on 2TU [2,35,36], we attribute the 69 amu fragment ion to  $C_3NH_3O^+$ , appearing due to the loss of (H)NCS rather than (H)NCO. This suggests that the fragmentation observed here, is more dependent on the nature of the pyrimidine ring, than on the position/substitution of the O/S atoms.

Experiments on deuterated uracil by Ryszka *et al.* strongly suggest that the 42 amu fragment ion of uracil is  $C_2H_2O^+$  [38], and has been similarly attributed in other studies [2,35,37,49,52–54]. This additional evidence from deuterated studies reduces the likelihood that the 42 amu fragment is the less often attributed  $NCO^+$  ion [51]. Due to the similarities between the molecules, we attribute the 42 amu fragment ion of 2TU to  $C_2H_2O^+$ .

Table 1 highlights that the appearance energy for the 41 amu fragment ion is lower than the 42 amu fragment ion. As already noted with the 95 and 96 amu fragment ions, this feature suggests that difference between the 41 and 42 amu fragment ions is unlikely to be a simple hydrogen loss after 42 amu

fragment formation. With this in mind, and after consulting a number of uracil studies [37,38,49,52–54], we attribute the 41 amu, at least in its majority, to  $C_2NH_3^+$ .

The deuterated-uracil studies of Ryszka *et al.* suggest that the 28 amu fragment ion is  $HCNH^+$  [38], which has been backed by several other studies [2,37,52,53]. We give the same attribution to the 28 amu fragment seen from 2TU.

In the case of the 42, 41 and 28 amu fragments, there is the possibility that they could be attributed to other atomic compositions, namely,  $NCO^+$ ,  $HCCO^+$  and  $CO^+$ , respectively, and have been done so in past works on uracil [51,52]. However, these attributions are very much in the minority for uracil and have been superseded by stronger arguments in our own reasoning and the other studies referenced above. We expect the attributions for fragments of 2TU detailed above to be the dominant fragments for each ion observed, and any attributions that may come from other fragments will not significantly contribute to the overall signal observed.

### 3.3. Parent ion UV/UV discussions

In Subsection 2.3., we showed that the parent ion was two-photon dependent at all pump-probe time delays. Combining this with the results seen in Subsection 2.5., where the same signal was observed in the pump-probe and probe-pump measurements despite using unequal laser intensities in each beam solidifies the idea the time-dependent signal for the parent ion presented in Subsection 2.4. is the result of a [1+1'] resonance-enhanced multiphoton ionization (REMPI) process.

From the fits of parent-ion pump-probe data presented in Subsection 2.4., we determined that the observed signal tended to the two-photon auto-correlation signal (430 fs). After reviewing the literature, this is what one would expect when exciting to the  $S_2$  ( $^1\pi_s\pi_s^*$ ) state [27], as this has been shown to decay in part directly to the ground state within 200 fs [34], and in part to the  $S_1$  with a sub-100 fs lifetime [2,24,26,29,31]. For the latter references, the claim is that the  $S_1$  relaxation is dominant, yet a direct  $S_2 \rightarrow S_0$  decay would explain how the signal returns efficiently to the background level. Additionally, the fact that the expected lifetime of this path is significantly shorter than our 300 fs pulses, would explain why the observed signal tends to that of the laser auto-correlation signal. Similarly, the  $S_2 \rightarrow S_1$  decay is also expected to be significantly shorter than the duration of our laser pulses, hence why the signal would also tend to the auto-correlation signal for this path. Yet, when the  $S_2 \rightarrow S_1$  path is chosen, one would also expect to see signals relating to the longer-lived  $S_1 \rightarrow$  Triplet manifold and Triplet  $\rightarrow$  Ground decays - except this is not observed for the parent ion. However, potential energy surface calculations and experimental photoelectron studies by the Ullrich group show that as the excited system propagates towards to the  $S_2$  minima there is a rapid increase in the ionization energy of molecule to around  $\sim 9.7$  eV, and it is not expected to drop back down below this as it passes through the  $S_1$  and tertiary states [24,29,31]. This means that the energy gap between the initial excitation and the ionization states is now larger than what a single photon of 266 nm light can provide, and hence it is no longer possible to produce the parent ion through a [1+1'] REMPI processes. Other pump-probe ion mass spectroscopy experiments have been similarly insensitive to longer decays, such as those of Ghafur *et al.* investigating the triplet decay of uracil [2]. It is unfortunately not possible to probe via the parent ion through a [1+2'] photon process, as results from Subsections 2.2., 2.3. and 2.5. show that this will favor the production of fragment ions instead. All of this explains why we are only able to observe a signal that tends towards the auto-correlation signal for the parent ion. We do, however, note that other experiments have followed the dynamics of the parent ion beyond the  $S_2$  decay using multi-photon probes with low-energy photons [2], as well as single-photon probe studies with probe energies above  $\sim 5.0$  eV [24]; this was not possible in our experiment.

### 3.4. Fragment ion UV/UV Photon-order processes

In Subsection 2.3., we showed that all of the fragment ions are produced in a three-photon process when using 266 nm light at all pump probe delays, except for the 28 amu ion, which is created in a three-photon process at time zero and proceeds as a four-photon process at all other delays. In Subsection 2.5., a stronger signal is observed for the 69 amu fragment ion when a weaker pulse is used to pump and a stronger pulse is used to probe. These points together, suggest that the 69 amu fragment ion is produced *via* a [1+2'] REMPI process, and, importantly, that the dynamics probed relate to dynamics on the excited neutral system. A reduction of the 69 amu fragment ion signal when a more intense laser is

used to excite the system, may also be indicative of rapid relaxations taking place in the cationic states, which prevent further photon absorption at 266 nm, of which similar conclusions have been drawn for the cationic states of uracil in the past [61].

Unfortunately, similar conclusions for the 41, 42 and 95 amu fragment ions cannot be drawn due to conflicting results. In first instances, the results presented in the Supplementary Data for these fragment ions suggest that a signal is only observed when the pump has a larger power than the probe, defining pump as the first pulse on the right hand side of the delay dependent scans. From this we *could* draw the conclusion that the observed signal for these ions originates from a [2+1'] REMPI process. However, counter to this, is that in the same plots we observe no difference between the pump-probe and probe-pump signals. If it was a [2+1'] REMPI process, we would expect to see little to no signal when the weaker probe beam comes first; yet no difference is observed. Because of this dichotomy, we cannot explicitly state if the signals observed for these ions relate to a [2+1'] or a [1+2'] REMPI process, and therefore subsequently if they relate to dynamics on the excited neutral system or the ion. An experiment that could potentially clear this issue, but was not possible to perform here, would be to perform pump-probe experiments in which the pump and probe beams possess different photon energies: one with pulse centred at 266 nm, and the other with a higher photon energy, tuned to allow for ionisation of certain states after excitation. Similarly, in the case of the 28 amu fragment, the results presented in the Supplementary Data relating to Subsection 2.5. do not allow us to conclude if the dynamics relate to a [1+3'], a [2+2'] or a [3+1'] REMPI process outside of the pump-probe overlap. Despite these shortcomings we will continue to draw conclusions from the results for these fragment ions as best as we can.

One of the most interesting observations from Subsection 2.3. was the change in the photon-order from 3 to 4 from the 28 amu fragment ion when moving away from the pump-probe temporal overlap. This three-photon process at time zero agrees well with the appearance energy of the 28 amu fragment determined in Subsection 2.2. of  $(14.04 \pm 0.02)$  eV, which is around the same energy of what is provided by three photons of 266 nm light,  $(13.98 \pm 0.05)$  eV. The increase in the photon order as we move away from time zero, likely indicates that within the first 100 fs after molecular excitation the energy gap between the pumped state and the ionization state needed to produce the 28 amu fragment widens along the path of the vibrational wavepacket. This is similar to our argument for the parent ion, and as seen in past experiments for 2TU [29] and uracil [4,49]. Unfortunately, due to the unclear results of Subsection 2.5., we cannot with certainty state if the widening of this gap is occurring between the neutral excited system and the ionisation states, or between the different cationic states.

### 3.5. Fragment ion UV/UV time-dependent signals

We will start this section with a discussion of the time-dependent signal of the 69 amu fragment ion, due to its clear [1+2'] REMPI nature. For this ion, we found that  $\tau_1$  tended towards zero, ultimately matching the shape of the auto-correlation signal. We attribute this to an ultrafast decay that is significantly shorter than the duration of the auto-correlation of the laser, and hence refer to  $\tau_1$  as a sub-370 fs feature (based on the width of three-photon auto-correlation signal). This is similar to what was observed with the parent ion, and like in the parent ion case, we attribute  $\tau_1$  to either the direct  $S_2 \rightarrow S_0$  decay or the  $S_2 \rightarrow S_1$  decay.

The  $\tau_2$  decay of the 69 amu ion was found to have a duration of  $417 \pm 321$  fs. This agrees with past studies that suggest the  $S_1 \rightarrow$  triplet-manifold decay should have a lifetime in the region of 200-800 fs when photons in the range of 240-300 nm are used to excite the system [2,24,26,29,31].

In the past, the lifetime of the lowest-energy triplet state of 2TU returning to the electronic ground state has been measured to be between ~50 ps to over 200 ps, as noted in Ref. [31]. This, however, was shown to be dependent on the excitation energy used, and corresponds to ~90 ps when ~266 nm light is used – this includes the parent-focussed results of the similar photo-ion probing experiments of Ghafur *et al.* [2]. We note that the  $\tau_3$  decay of the 69 amu fragment ion was fitted to  $(309 \pm 25)$  ps, which is significantly longer than the reported parent ion decay. With this in mind, we highlight the strong-field ionization experiments of uracil by Kotur *et al.*, where a 2.2 ps decay was observed for the parent ion, but a range of decays from 1.5 to 3.5 ps was observed for the fragments [4]. Kotur *et al.* suggested that the spread may be an indication of a delocalization of the wavepacket somewhere in the relaxation process, and leads to multiple decay paths. Those could be observed at different points in the potential

energy landscape by different probe mechanisms as different time constants. It is possible that a similar process is also observed here for 2TU.

In Table 3, we can see that the 28, 41, 69 and 95 fragment ions all share similar fitted decay constants. All of the  $\tau_1$  constants tend towards zero, all values for  $\tau_2$  fall in the region of 300-450 fs, and all of the  $\tau_3$  constants fall in the range of 220 to 400 ps. Due to the similar decay constants between all of the ions, we believe that this is indicative that the decay constants are representative of the same decay mechanisms. That is to say, we believe that all of the fragment ions discussed here follow the same decay process to that ascribed to the 69 amu fragment ion; i.e.  $\tau_1$  is the  $S_2 \rightarrow S_0 / S_2 \rightarrow S_1$  decay,  $\tau_2$  is the  $S_1 \rightarrow$  Triplet-manifold decay, and  $\tau_3$  is the Triplet Manifold  $\rightarrow$  ground state decay. This therefore implies that the signals observed for these fragment ions are representative of the dynamics of the neutral excited state and not the ion. However, as this conclusion is based on coincidence, we cannot explicitly confirm this due to ambiguities noted in Subsections 2.5. and 3.4.

Finally, the 42 amu ion appears to be somewhat of an outlier for all of the ions we discuss here as no unique  $\tau_2$  decay could be fitted. In Table 3, we can see that for all of the other fragment ions the value of  $\tau_2$  varies slightly, yet are on the same order of magnitude as the three-photon autocorrelation signal (370 fs). We therefore suspect that the  $\tau_2$  decay is still present for the 42 amu ion, however, that it may be sufficiently shorter than the other  $\tau_2$  values so as to be obscured by the relatively wide auto-correlation signal. Therefore, formally, we attribute the  $\tau_1$  decay of the 42 amu ion to an overlap of the  $S_2 \rightarrow S_0 / S_2 \rightarrow S_1$  decay and the  $S_1 \rightarrow$  Triplet-manifold decay, whilst the  $\tau_3$  decay for the 42 amu ion still represents the Triplet Manifold  $\rightarrow$  ground state decay.

## 4. Materials and Methods

### 4.1. UV/UV Pump-Probe experiments

In this section, we provide a general overview of the set-up used in the UV/UV pump-probe experiments. As noted previously, specific parameters to each of the experiments discussed in the results section are summarised at the beginning of each respective subsection.

Figure 6 shows a simplified version of the experimental set-up used in the UV/UV studies, and is similar to the set-up used in previously published experiments [45]. In this, a 1 W, 1 kHz, 35 fs, 800 nm beam from a Ti:Sapphire laser is directed through a third harmonic generation (THG) set-up. The UV pulse energy is controlled by detuning the input beam polarization with respect to the THG set-up *via* the rotation of a  $\lambda/2$  plate situated before the THG set-up. After generation, the filtered third-harmonic light passes through a Michelson interferometer to produce collinear pump and probe beams, of which the delay between the two beams is controlled *via* a motorised translation stage. With the interferometer described so far, pump and probe beams of equal powers will be produced; this is the set-up used in Subsections 2.1., 2.3. and 2.4. For results relating to those seen in Subsection 2.5., variable ND filters were inserted into the individual arms of the Michelson interferometer, allowing for the production of pump and probe beams with individually controlled pulse energies. After the interferometer, the beams are directed towards the vacuum apparatus *via* a number of reflectors and focussing optics. The spot size of the UV laser beams was measured to be approximately 30  $\mu\text{m}$  in diameter. A power meter positioned directly at an exit viewport of the apparatus (after the laser is focussed in the chamber) was used to measure the power of the laser for each data point collected.

Inside the vacuum apparatus, the sample capillary oven [62] is positioned using a three-axis linear manipulator over the path of the pump and probe beams, with the tip of the delivery needle sitting  $\sim$ 1-2 mm above the laser focus. As molecules leave the oven, they are ionized by the laser pulses and detected *via* a Time-of-Flight (ToF) mass spectrometer based on the Wiley-McLaren design [63] using micro-channel-plate detectors. The ToF traces are read out using an oscilloscope. All data from the oscilloscope are transferred to a computer, where all traces are recorded. The repeller and extractor plates of the Wiley-McLaren electron-optics are held at +900 and -900 V, respectively, and are situated 30 mm apart. The 180 mm long flight tube starts 10 mm behind the extractor and is set to -1600 V to further accelerate the ions. Voltages on each component were slightly tuned while keeping differences constant to optimize resolution. Achievable mass resolution of the spectrometer assembly was about 150.

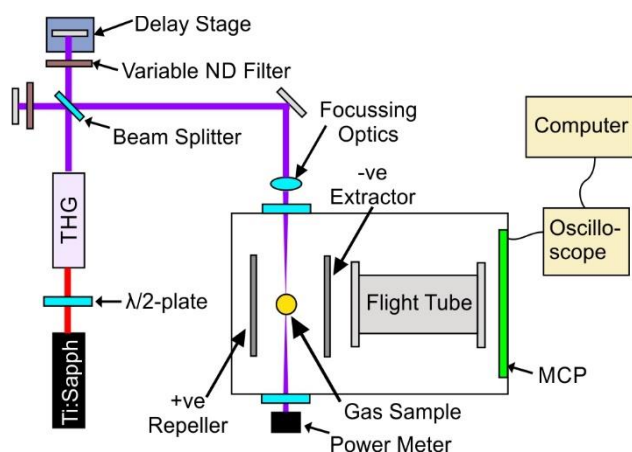


**Figure 6.** Simplified sketch of the experimental set-up, showing a Michelson interferometer creating pump and probe pulses with controlled delay from the third-harmonic (266 nm) of a Ti:Sapphire laser. Variable ND filters sit in each arm of the interferometer, allowing for pump and probe beams with differing powers to be utilised. After the interferometer, the laser beams are directed into the ion mass spectrometer, where they cross with an effusive beam of 2TU (produced from a heated capillary oven [62]), to induce ionization. These ions are accelerated *via* an electric potential across extraction plates towards an MCP detector through a flight tube, where their  $m/q$ -dependent arrival time is observed on an oscilloscope and recorded on a computer.

2-Thiouracil was obtained from Sigma-Aldrich (purity  $\geq 99\%$ ) and used without further refinement. The capillary oven was heated to 190 °C, which is below the temperature used in other experiments, and so we are confident that we are not at the decomposition threshold [24,28,31]. The nozzle of the oven is heated to 200°C to prevent sample delivery blockages. This produced a typical sample density of  $1 \times 10^{12}$  molecules/cm<sup>3</sup> at the point where laser beams cross with the gas flow [62].

The pulse duration of the UV laser was obtained by recording the time-resolved mass spectra of different gases backfilled into the apparatus through a needle valve, whose output was situated near the focus of the pump and probe beams. These measurements were performed with the variable ND filters seen in Figure 6 removed. The gases used were 1,4-dioxane and xenon, which are ionised *via* a two- and three-photon non-resonant process, respectively, when using 266 nm photons [64,65]. The time-dependent parent ion signals for 1,4-dioxane and xenon were fitted to a Gaussian curve with full-width half-maxima (FWHM) of 430 and 370 fs, respectively. Both tests suggest a pulse duration of 300 fs. Through fits of data seen in Section 3E, we estimate that the pulses are stretched to  $\sim 500$  fs with the aforementioned ND filters in place. The stretching of the pulse will not affect the observed dynamics for the time constants discussed here.

Data were collected with both the pump and probe beams entering the chamber in a “laser-on/laser-off” fashion. For each laser-on data point collected, a laser-off data point was collected immediately afterwards, before moving to the next data point. This allows for improved background correction. In addition, runs which relate to pump-only and probe-only signals were also collected, allowing for “pump-/probe-only” Vs “pump-probe” signals to be compared where necessary. Data was collected in a series of “loops”. For each loop, data for the full combination of pump-probe delays and laser powers of interest was collected in a randomized order, before the process was repeated for the next loop. This method helps to reduce the effect of slow drifts, whilst the combination of small instabilities in the interferometer and the multiple samples taken help to reduce interference effects between the pump and probe beams around time zero. In the power series of Subsection 2.3, a total of 24,000 laser shots per data point were collected over the course of 8 loops. In the pump-probe scans of Subsection 2.4, data representing 50,000 laser shots per data point collected over 16 Loops for the “low-power” scan, over the delay range of  $-1 \rightarrow 1$  ps. In the “high-power” scan performed over  $-3 \rightarrow 15$  ps, 250,000 laser shots per data point were collected over 50 Loops, whilst in the “high-power” scan over the range of  $0 \rightarrow 100$  ps, 60,000 laser shots per data point were collected over 12 Loops. Finally, in the non-equal pump-probe experiments of Subsection 2.5., data was collected over 10 loops with a total of 14,000 laser shots being collected per data point.

The laser powers used depended on the experiment being performed, and exact values are detailed as appropriate in the following sections. However, in general, experimental pulse energies were measured to be between 0.5-15 ( $\pm 5\%$ ) nJ per beam, providing a beam intensity in the range of  $2 \times 10^8$  -  $7 \times 10^9$  W/cm<sup>2</sup> per beam at the interaction region.

#### 4.2 VUV dissociative photoionization experiments

The VUV dissociative photoionization data were collected at the VUV beamline of the SLS. The instrument for our study utilises a double velocity-map-imaging photoelectron photoion coincidence ('PEPICO') spectrometer to detect ions produced by a sample coming into contact with a quasi-continuous-wave monochromatized synchrotron light source [66–69]. Specifically, we selectively observe ions that arrive in coincidence to near zero-kinetic energy electrons (circa.  $<10$  meV), allowing us to study threshold-ionized ions (i.e. threshold photoelectron photoion coincidence spectroscopy). Ultimately, this allows for the determination of the appearance energies of the ions of interest. The same 2TU sample described in the UV/UV experiment was used here, introduced into the path of the VUV light *via* a filled ampule heated to 150°C, and directed towards the interaction region *via* a thin nozzle.

Data was collected in three runs, each over a different range of photon energies, which include: 1)  $h\nu = 8 \rightarrow 12$  eV in 10 meV steps, 2)  $h\nu = 11 \rightarrow 15$  eV in 20 meV steps and 3)  $h\nu = 12 \rightarrow 20$  eV in 40 meV steps. Whilst data up to 20 eV photon energy was recorded, only data in the  $h\nu = 8.55$ -15 eV range is presented in this paper, as this is sufficient to assist in the analysis of the UV/UV experiments. The data presented in Figure 2 is stitched together from the three runs, explicitly using data from run 1) in the range  $h\nu = 8.55 \rightarrow 11.5$  eV, run 2) in the range  $h\nu = 11.5 \rightarrow 14$  eV, and run 3) in the range  $h\nu = 14 \rightarrow 15$  eV. Switch-over points were chosen to account for both signal strength and effects of the gas filter of the beamline [69]. The smallest step size of 10 meV approximately matches the bandwidth of the monochromatic beam [66]. This collection method produced a fine scan over the region where ions of interest would start to appear, as well as provide sufficient overlap between each run, allowing for normalization of signal between runs, and accounting for changes of gas filters in the beamline [69]. For each data point 180 seconds worth of data was collected.

## 5. Conclusions

In this work, through the combination of time-resolved UV/UV pump-probe data and VUV PEPICO data, we have been able to gain a deeper understanding of the excited-state dynamics of 2TU and its photo-induced dissociation. We have been able to use experimental evidence from two different techniques to provide reasoning as to why different photon orders are needed for the production of different ions. In the case of the 28 amu fragment ion, we were also able to provide reasoning as to why this photon order changes once a delay is introduced between the pump and probe beams.

Additionally, in fitting the time-dependent signals of the fragment ions, we find that their decay constants match well to the previously established  $S_2 \rightarrow S_1 \rightarrow \text{Triplet manifold} \rightarrow \text{ground state}$  decay route for 2TU, with the hint that the exact Triplet manifold  $\rightarrow$  ground state decay constant may be fragment specific.

We have also highlighted and discussed the origin of several fragment ions, such as the difference between the 95 and 96 amu ions, which may in the future prove useful in identifying the differences in the dynamics between 2TU and uracil, as well as 4-thiouracil and 2,4-dithiouracil.

Overall, the results presented here provide information on the higher-lying ionisation states of 2TU, and, to a degree how, they evolve as 2TU decays from the  $S_2$  state. This information will be useful for future theoretical models of 2TU that concentrate on these states, as well as other (thio)uracils and DNA/RNA nucleobases.

**Supplementary Materials:** The following are available online at [www.mdpi.com/xxx/s1](http://www.mdpi.com/xxx/s1), Figure S1: Power series for the 28 amu fragment ion., Figure S2: Power series for the 41 amu fragment ion., Figure S3: Power series for the 42 amu fragment ion., Figure S4: Power series for the 69 amu fragment ion., Figure S5: Power series for the 95 amu fragment ion., Figure S6: Power series for the parent (128 amu) ion., Figure S7: Time-dependent decay of the 41 amu fragment ion., Figure S8: Time-dependent decay of the 42 amu fragment ion., Figure S9: Time-dependent decay of the 95 amu fragment ion., Figure S10: Inhomogenous pump-probe signal for the 28 amu fragment ion., Figure S11: Inhomogenous pump-probe signal for the 41 amu fragment ion., Figure S12: Inhomogenous pump-probe signal for the 42 amu fragment ion., Figure S13: Inhomogenous pump-probe signal for the 95 amu fragment ion. Additionally, there is a discussion of the "Novelties of the 100 amu fragment".

**Acknowledgments:** We thank P. Hemberger and A. Bodi for support during the SLS beamtime.

**Author Contributions:** Conceptualization, M.S.R., M.N. and M.G.; methodology, M.S.R., M.N. and M.G.; software, M.N.; validation, M.S.R., M.N. and M.G.; formal analysis, M.S.R.; investigation, M.S.R. and M.N.; resources, M.G.; data curation, M.S.R. and M.N.; writing—original draft preparation, M.S.R.; writing—review and editing, M.S.R., M.N. and M.G.; visualization, M.S.R. and M.N.; supervision, M.G.; project administration, M.G.; funding acquisition, M.G. All authors have read and agreed to the published version of the manuscript.

**Funding:** We acknowledge the Paul Scherrer Institut, Villigen, Switzerland for provision of synchrotron radiation beamtime at beamline X04DB of the SLS, during proposal 20171655. The group is funded by a Lichtenberg Professorship of the Volkswagen Foundation. We acknowledge funding from the DFG through grant INST 336/112-1.

## References

1. Barc, B.; Ryszka, M.; Spurrell, J.; Dampc, M.; Limão-Vieira, P.; Parajuli, R.; Mason, N.J.; Eden, S. Multi-photon ionization and fragmentation of uracil: Neutral excited-state ring opening and hydration effects. *J. Chem. Phys.* **2013**, *139*, doi:10.1063/1.4851476.
2. Ghafur, O.; Crane, S.W.; Ryszka, M.; Bockova, J.; Rebelo, A.; Saalbach, L.; De Camillis, S.; Greenwood, J.B.; Eden, S.; Townsend, D. Ultraviolet relaxation dynamics in uracil: Time-resolved photoion yield studies using a laser-based thermal desorption source. *J. Chem. Phys.* **2018**, *149*, 034301, doi:10.1063/1.5034419.
3. González-Vázquez, J.; González, L.; Samoylova, E.; Schultz, T. Thymine relaxation after UV irradiation: The role of tautomerization and  $\pi\sigma^*$  states. *Phys. Chem. Chem. Phys.* **2009**, *11*, 3927–3934, doi:10.1039/b815602f.
4. Kotur, M.; Weinacht, T.C.; Zhou, C.; Matsika, S. Following Ultrafast Radiationless Relaxation Dynamics With Strong Field Dissociative Ionization: A Comparison Between Adenine, Uracil, and Cytosine. *IEEE J. Sel. Top. QUANTUM Electron.* **2012**, *18*, 187–194, doi:10.1109/JSTQE.2011.2107892.
5. Wolf, T.J.A.; Parrish, R.M.; Myhre, R.H.; Martínez, T.J.; Koch, H.; Gühr, M. Observation of ultrafast intersystem crossing in thymine by extreme ultraviolet time-resolved photoelectron spectroscopy. *J. Phys. Chem. A* **2019**, *123*, 6897–6903, doi:10.1021/acs.jpca.9b05573.
6. M. Barbatti, A. C. Borin, S.U. *Photoinduced Phenomena in Nucleic Acids Top. Curr. Chem.* 355; Springer, 2015;
7. Crespo-Hernández, C.E.; Cohen, B.; Hare, P.M.; Kohler, B. Ultrafast excited-state dynamics in nucleic acids. *Chem. Rev.* **2004**, *104*, 1977–2019, doi:10.1021/cr0206770.
8. Cui, G.; Fang, W.H. State-specific heavy-atom effect on intersystem crossing processes in 2-thiothymine: A potential photodynamic therapy photosensitizer. *J. Chem. Phys.* **2013**, *138*, doi:10.1063/1.4776261.
9. Attard, N.R.; Karran, P. UVA photosensitization of thiopurines and skin cancer in organ transplant recipients. *Photochem. Photobiol. Sci.* **2012**, *11*, 62–68, doi:10.1039/c1pp05194f.
10. Schreier, W.J.; Gilch, P.; Zinth, W. Early events of DNA photodamage. *Annu. Rev. Phys. Chem.* **2015**, *66*, 497–519, doi:10.1146/annurev-physchem-040214-121821.
11. Middleton, C.T.; De La Harpe, K.; Su, C.; Law, Y.K.; Crespo-Hernández, C.E.; Kohler, B. DNA excited-state dynamics: From single bases to the double helix. *Annu. Rev. Phys. Chem.* **2009**, *60*, 217–239, doi:10.1146/annurev.physchem.59.032607.093719.
12. Crespo-Hernández, C.E.; Cohen, B.; Kohler, B. Base stacking controls excited-state dynamics in A-T DNA. *Nature* **2005**, *436*, 1141–1144, doi:10.1038/nature03933.
13. Kneuttinger, A.C.; Kashiwazaki, G.; Prill, S.; Heil, K.; Carell, T. Formation and direct repair of UV-induced dimeric



DNA pyrimidine lesions. *Photochem. Photobiol.* **2014**, *90*, 1–14, doi:10.1111/php.12197.

14. *Photoinduced Phenomena in Nucleic Acids I Nucleobases in the Gas Phase and in Solvents*; Mario Barbatti, Antonio Carlos Borin, S.U., Ed.; Springer International Publishing, 2015; ISBN 978-3-319-13370-6.
15. Zechmann, G.; Barbatti, M. Photophysics and deactivation pathways of thymine. *J. Phys. Chem. A* **2008**, *112*, 8273–8279, doi:10.1021/jp804309x.
16. Arslançan, S.; Martínez-Fernández, L.; Corral, I. Photophysics and photochemistry of canonical nucleobases' thio-analogs: From quantum mechanical studies to time resolved experiments. *Molecules* **2017**, *22*, 998, doi:10.3390/molecules22060998.
17. Pollum, M.; Martínez-Fernández, L.; Crespo-Hernández, C.E. Photochemistry of nucleic acid bases and their thio- and aza-analogues in solution. *Top. Curr. Chem.* **2015**, *355*, 245–327, doi:10.1007/128\_2014\_554.
18. Bai, S.; Barbatti, M. On the decay of the triplet state of thionucleobases. *Phys. Chem. Chem. Phys.* **2017**, *19*, 12674–12682, doi:10.1039/C7CP02050C.
19. Pollum, M.; Jockusch, S.; Crespo-Hernández, C.E. Increase in the photoreactivity of uracil derivatives by doubling thionation. *Phys. Chem. Chem. Phys.* **2015**, *17*, 27851–27861, doi:10.1039/c5cp04822b.
20. Martínez-Fernández, L.; Granucci, G.; Pollum, M.; Crespo-Hernández, C.E.; Persico, M.; Corral, I. Decoding the Molecular Basis for the Population Mechanism of the Triplet Phototoxic Precursors in UVA Light-Activated Pyrimidine Anticancer Drugs. *Chem. - A Eur. J.* **2017**, *23*, 2619–2627, doi:10.1002/chem.201604543.
21. Park, E.; Baron, R.; Landgraf, R. Higher-order association states of cellular ERBB3 probed with photo-cross-linkable aptamers. *Biochemistry* **2008**, *47*, 11992–12005, doi:10.1021/bi8004208.
22. Brem, R.; Daehn, I.; Karran, P. Efficient DNA interstrand crosslinking by 6-thioguanine and UVA radiation. *DNA Repair (Amst)*. **2011**, *10*, 869–876, doi:https://doi.org/10.1016/j.dnarep.2011.05.010.
23. Mai, S.; Pollum, M.; Martínez-Fernández, L.; Dunn, N.; Marquetand, P.; Corral, I.; Crespo-Hernández, C.E.; González, L. The origin of efficient triplet state population in sulfur-substituted nucleobases. *Nat. Commun.* **2016**, *7*, 1–8, doi:10.1038/ncomms13077.
24. Mai, S.; Mohamadzade, A.; Marquetand, P.; González, L.; Ullrich, S. Simulated and experimental time-resolved photoelectron spectra of the intersystem crossing dynamics in 2-thiouracil. *Molecules* **2018**, *23*, doi:10.3390/molecules23112836.
25. Ruckebauer, M.; Mai, S.; Marquetand, P.; González, L. Photoelectron spectra of 2-thiouracil, 4-thiouracil, and 2,4-dithiouracil. *J. Chem. Phys.* **2016**, *144*, 074303, doi:10.1063/1.4941948.
26. Mai, S.; Marquetand, P.; González, L. Intersystem Crossing Pathways in the Noncanonical Nucleobase 2-Thiouracil: A Time-Dependent Picture. *J. Phys. Chem. Lett.* **2016**, *7*, 1978–1983, doi:10.1021/acs.jpcllett.6b00616.
27. Mai, S.; Marquetand, P.; González, L. A Static Picture of the Relaxation and Intersystem Crossing Mechanisms of Photoexcited 2-Thiouracil. *J. Phys. Chem. A* **2015**, *119*, 9524–9533, doi:10.1021/acs.jpca.5b06639.
28. Mayer, D.; Picconi, D.; Robinson, M.S.; Gühr, M. Experimental and theoretical gas-phase absorption spectra of thionated uracils. *Chem. Phys.* **2022**, *558*, 111500, doi:10.1016/j.chemphys.2022.111500.
29. Yu, H.; Sanchez-Rodriguez, J.A.; Pollum, M.; Crespo-Hernández, C.E.; Mai, S.; Marquetand, P.; González, L.; Ullrich, S. Internal conversion and intersystem crossing pathways in UV excited, isolated uracils and their implications in prebiotic chemistry. *Phys. Chem. Chem. Phys.* **2016**, *18*, 20168–20176, doi:10.1039/c6cp01790h.

30. Pollum, M.; Crespo-Hernández, C.E. Communication: The dark singlet state as a doorway state in the ultrafast and efficient intersystem crossing dynamics in 2-thiothymine and 2-thiouracil. *J. Chem. Phys.* **2014**, *140*, 071101, doi:10.1063/1.4866447.
31. Sánchez-Rodríguez, J.A.; Mohamadzade, A.; Mai, S.; Ashwood, B.; Pollum, M.; Marquetand, P.; González, L.; Crespo-Hernández, C.E.; Ullrich, S. 2-Thiouracil intersystem crossing photodynamics studied by wavelength-dependent photoelectron and transient absorption spectroscopies. *Phys. Chem. Chem. Phys.* **2017**, *19*, 19756–19766, doi:10.1039/c7cp02258a.
32. Ullrich, S.; Mohamadzade, A. Intersystem crossing dynamics in thionated uracils studied by time-resolved photoelectron spectroscopy: The effect of substituent position. *EPJ Web Conf.* **2019**, *205*, 09010, doi:10.1051/epjconf/201920509010.
33. Lever, F.; Mayer, D.; Picconi, D.; Metje, J.; Alisauskas, S.; Calegari, F.; Düsterer, S.; Ehlert, C.; Feifel, R.; Niebuhr, M.; et al. Ultrafast dynamics of 2-thiouracil investigated by time-resolved Auger spectroscopy. *J. Phys. B At. Mol. Opt. Phys.* **2020**, *54*, 014002, doi:10.1088/1361-6455/abc9cb.
34. Mayer, D.; Lever, F.; Picconi, D.; Metje, J.; Alisauskas, S.; Calegari, F.; Düsterer, S.; Ehlert, C.; Feifel, R.; Niebuhr, M.; et al. Following excited-state chemical shifts in molecular ultrafast x-ray photoelectron spectroscopy. *Nat. Commun.* **2022**, *13*, 198, doi:10.1038/s41467-021-27908-y.
35. Hecht, S.M.; Gupta, A.S.; Leonard, N.J. Position of uridine thiation: The identification of minor nucleosides from transfer RNA by mass spectrometry. *BBA Sect. Nucleic Acids Protein Synth.* **1969**, *182*, 444–448, doi:10.1016/0005-2787(69)90195-6.
36. Uleanya, K.O.; Cercola, R.; Nikolova, M.; Matthews, E.; Wong, N.G.K.; Dessent, C.E.H. Observation of Enhanced Dissociative Photochemistry in the Non-Native Nucleobase 2-Thiouracil. *Molecules* **2020**, *25*, 15–17, doi:10.3390/molecules25143157.
37. Jochims, H.W.; Schwell, M.; Baumgärtel, H.; Leach, S. Photoion mass spectrometry of adenine, thymine and uracil in the 6–22 eV photon energy range. *Chem. Phys.* **2005**, *314*, 263–282, doi:10.1016/j.chemphys.2005.03.008.
38. Ryszka, M.; Pandey, R.; Rizk, C.; Tabet, J.; Barc, B.; Dampc, M.; Mason, N.J.; Eden, S. Dissociative multi-photon ionization of isolated uracil and uracil-adenine complexes. *Int. J. Mass Spectrom.* **2016**, *396*, 48–54, doi:10.1016/j.ijms.2015.12.006.
39. Majer, K.; Signorell, R.; Heringa, M.F.; Goldmann, M.; Hemberger, P.; Bodi, A. Valence Photoionization of Thymine: Ionization Energies, Vibrational Structure, and Fragmentation Pathways from the Slow to the Ultrafast. *Chem. - A Eur. J.* **2019**, *25*, 14192–14204, doi:10.1002/chem.201903282.
40. Asher, R.L.; Appelman, E.H.; Ruscic, B. On the heat of formation of carbonyl fluoride, CF<sub>2</sub>O. *J. Chem. Phys.* **1996**, *105*, 9781–9795, doi:10.1063/1.436160.
41. Di Giacomo, F. A short account of RRKM theory of unimolecular reactions and of marcus theory of electron transfer in a historical perspective. *J. Chem. Educ.* **2015**, *92*, 476–481, doi:10.1021/ed5001312.
42. Sztáray, B.; Bodi, A.; Baer, T. Modeling unimolecular reactions in photoelectron photoion coincidence experiments. *J. Mass Spectrom.* **2010**, *45*, 1233–1245, doi:10.1002/jms.1813.
43. L'Huillier, A.; Lompre, L.A.; Mainfray, G.; Manus, C. Multiply charged ions induced by multiphoton absorption in rare gases at 0.53  $\mu\text{m}$ . *Phys. Rev. A* **1983**, *27*, 2503–2512, doi:10.1103/PhysRevA.27.2503.

44. Koch, M.; Wolf, T.J.A.; Gühr, M. Understanding the modulation mechanism in resonance-enhanced multiphoton probing of molecular dynamics. *Phys. Rev. A - At. Mol. Opt. Phys.* **2015**, *91*, 1–5, doi:10.1103/PhysRevA.91.031403.
45. Robinson, M.S.; Niebuhr, M.; Lever, F.; Mayer, D.; Metje, J.; Guehr, M. Ultrafast Photo-Ion Probing of the Ring-Opening Process in Trans-Stilbene Oxide. *Chem. – A Eur. J.* **2021**, *27*, 11418, doi:10.1002/chem.202101343.
46. Katritzky, A.R.; Szafran, M.; Pfister-Guillouzo, G. The tautomeric equilibria of thio analogues of nucleic acid bases. Part 3. Ultraviolet photoelectron spectra of 2-thiouracil and its methyl derivatives. *J. Chem. Soc. Perkin Trans. 2* **1990**, 871, doi:10.1039/p29900000871.
47. Page, R.H.; Larkin, R.J.; Shen, Y.R.; Lee, Y.T. High-resolution photoionization spectrum of water molecules in a supersonic beam. *J. Chem. Phys.* **1988**, *88*, 2249–2263, doi:10.1063/1.454058.
48. Tonkyn, R.G.; Winniczek, J.W.; White, M.G. Rotationally resolved photoionization of O<sub>2</sub><sup>+</sup> near threshold. *Chem. Phys. Lett.* **1989**, *164*, 137–142, doi:10.1016/0009-2614(89)85005-5.
49. Matsika, S.; Zhou, C.; Kotur, M.; Weinacht, T.C. Combining dissociative ionization pump-probe spectroscopy and ab initio calculations to interpret dynamics and control through conical intersections. *Faraday Discuss.* **2011**, *153*, 247–260, doi:10.1039/c1fd00044f.
50. Denifl, S.; Sonnweber, B.; Hanel, G.; Scheier, P. Threshold electron impact ionization studies of uracil. *Int. J. of Mass Spectrom.* **2004**, *238*, 47–53, doi:10.1016/j.ijms.2004.07.010.
51. Coupier, B.; Farizon, B.; Farizon, M.; Gaillard, M.J.; Gobet, F.; De Castro Faria, N. V.; Jalbert, G.; Ouaskit, S.; Carré, M.; Gstir, B.; et al. Inelastic interactions of protons and electrons with biologically relevant molecules. *Eur. Phys. J. D* **2002**, *20*, 459–468, doi:10.1140/epjd/e2002-00166-3.
52. Rice, J.M.; Dudek, G.O.; Barber, M. Mass Spectra of Nucleic Acid Derivatives. Pyrimidines. *J. Am. Chem. Soc.* **1965**, *87*, 4569–4576, doi:10.1021/ja00948a029.
53. Nelson, C.C.; McCloskey, J.A. Collision-induced dissociation of uracil and its derivatives. *J. Am. Soc. Mass Spectrom.* **1994**, *5*, 339–349, doi:10.1016/1044-0305(94)85049-6.
54. Zhou, C.; Matsika, S.; Kotur, M.; Weinacht, T.C. Fragmentation pathways in the uracil radical cation. *J. Phys. Chem. A* **2012**, *116*, 9217–9227, doi:10.1021/jp209213e.
55. Uleanya, K.; Dessent, C.E.H. Investigating the Mapping of Chromophore Excitations onto the Electron Detachment Spectrum: Photodissociation Spectroscopy of Iodide Ion-Thiouracil Clusters. *Phys. Chem. Chem. Phys.* **2021**, *23*, 1021–1030, doi:10.1039/d0cp05920j.
56. Natalis, P.; Franklin, J.L. Ionization and dissociation of diphenyl and condensed-ring aromatics by electron impact. III. Azobenzene. *Int. J. Mass Spectrom. Ion Phys.* **1981**, *40*, 35–42, doi:10.1016/0020-7381(81)85004-8.
57. Castrovilli, M.C.; Trabattoni, A.; Bolognesi, P.; O’Keeffe, P.; Avaldi, L.; Nisoli, M.; Calegari, F.; Cireasa, R. Ultrafast Hydrogen Migration in Photoionized Glycine. *J. Phys. Chem. Lett.* **2018**, *9*, 6012–6016, doi:10.1021/acs.jpcllett.8b02089.
58. Giuliano, B.M.; Feyer, V.; Prince, K.C.; Coreno, M.; Evangelisti, L.; Melandri, S.; Caminati, W. Tautomerism in 4-hydroxypyrimidine, S-methyl-2-thiouracil, and 2-thiouracil. *J. Phys. Chem. A* **2010**, *114*, 12725–12730, doi:10.1021/jp106883s.
59. Kotur, M.; Weinacht, T.C.; Zhou, C.; Kistler, K.A.; Matsika, S. Distinguishing between relaxation pathways by combining dissociative ionization pump probe spectroscopy and ab initio calculations: A case study of cytosine. *J. Chem. Phys.* **2011**, *134*, doi:10.1063/1.3586812.

60. Wolf, T.; Holzmeier, F.; Wagner, I.; Berrah, N.; Bostedt, C.; Bozek, J.; Bucksbaum, P.; Coffee, R.; Cryan, J.; Farrell, J.; et al. Observing Femtosecond Fragmentation Using Ultrafast X-ray-Induced Auger Spectra. *Appl. Sci.* **2017**, *7*, 681, doi:10.3390/app7070681.
61. Assmann, M.; Köppel, H.; Matsika, S. Photoelectron spectrum and dynamics of the uracil cation. *J. Phys. Chem. A* **2015**, *119*, 866–875, doi:10.1021/jp512221x.
62. McFarland, B.K.; Berrah, N.; Bostedt, C.; Bozek, J.; Bucksbaum, P.H.; Castagna, J.C.; Coffee, R.N.; Cryan, J.P.; Fang, L.; Farrell, J.P.; et al. Experimental strategies for optical pump - Soft x-ray probe experiments at the LCLS. *J. Phys. Conf. Ser.* **2014**, *488*, 012015, doi:10.1088/1742-6596/488/1/012015.
63. Wiley, W.C.; McLaren, I.H. Time-Of-Flight Mass Spectrometer with Improved Resolution. *Rev. Sci. Instrum.* **1955**, *26*, 1150–1157.
64. Giugni, A.; Cavalieri, S.; Eramo, R.; Fini, L.; Materazzi, M. Electron angular distributions in non-resonant three-photon ionization of xenon. *J. Phys. B At. Mol. Opt. Phys.* **2000**, *33*, 285–289, doi:10.1088/0953-4075/33/2/312.
65. Okuno, T.; Imasaka, T.; Kida, Y.; Imasaka, T. Autocorrelator for measuring an ultrashort optical pulse width in the ultraviolet region based on two-photon ionization of an organic compound. *Opt. Commun.* **2014**, *310*, 48–52, doi:10.1016/j.optcom.2013.07.055.
66. Bodi, A.; Hemberger, P.; Gerber, T.; Sztáray, B. A new double imaging velocity focusing coincidence experiment: I2PEPICO. *Rev. Sci. Instrum.* **2012**, *83*, 083105, doi:10.1063/1.4742769.
67. Sztáray, B.; Voronova, K.; Torma, K.G.; Covert, K.J.; Bodi, A.; Hemberger, P.; Gerber, T.; Osborn, D.L. CRF-PEPICO: Double velocity map imaging photoelectron photoion coincidence spectroscopy for reaction kinetics studies. *J. Chem. Phys.* **2017**, *147*, doi:10.1063/1.4984304.
68. Bodi, A.; Sztáray, B.; Baer, T.; Johnson, M.; Gerber, T. Data acquisition schemes for continuous two-particle time-of-flight coincidence experiments. *Rev. Sci. Instrum.* **2007**, *78*, 084102, doi:10.1063/1.2776012.
69. Johnson, M.; Bodi, A.; Schulz, L.; Gerber, T. Vacuum ultraviolet beamline at the Swiss Light Source for chemical dynamics studies. *Nucl. Instruments Methods Phys. Res. Sect. A* **2009**, *610*, 597–603, doi:10.1016/j.nima.2009.08.069.

# Ultrafast photo-ion probing of the relaxation dynamics in 2-thiouracil: Supplementary Data

Here we present additional data and commentary from the UV/UV pump-probe ion mass spectroscopy experiments, to complement and expand the main article.

## 1. Power Series

The power series plots seen in Figures S1-S6 represent the full data set discussed in Subsection 2.3 of the main article, showing how the Signal for each ion of interest varies with respect to the combined pump-probe laser energy. The data is displayed in a “log-log” format and each figure is divided into six sections, representing data collected in the power series at different pump-probe delays, including a) Time zero, b) 100 fs, c) 500 fs, d) 1 ps, e) 5 ps and f) 10 ps. Main data points are shown as blue dots. The dotted red lines in each plot show the region in which the slope of  $\log_{10}(\text{Signal})$  Vs  $\log_{10}(\text{Laser Energy})$  was fitted. The resulting fit is then represented by the solid red line, with the value of the fitted gradient,  $m$ , being shown in the bottom right corner of each plot (the same value seen in Table 2 of the main article). Error bars outside of the fitting region have been excluded due to their unreliability caused by either a limited or saturated signal.

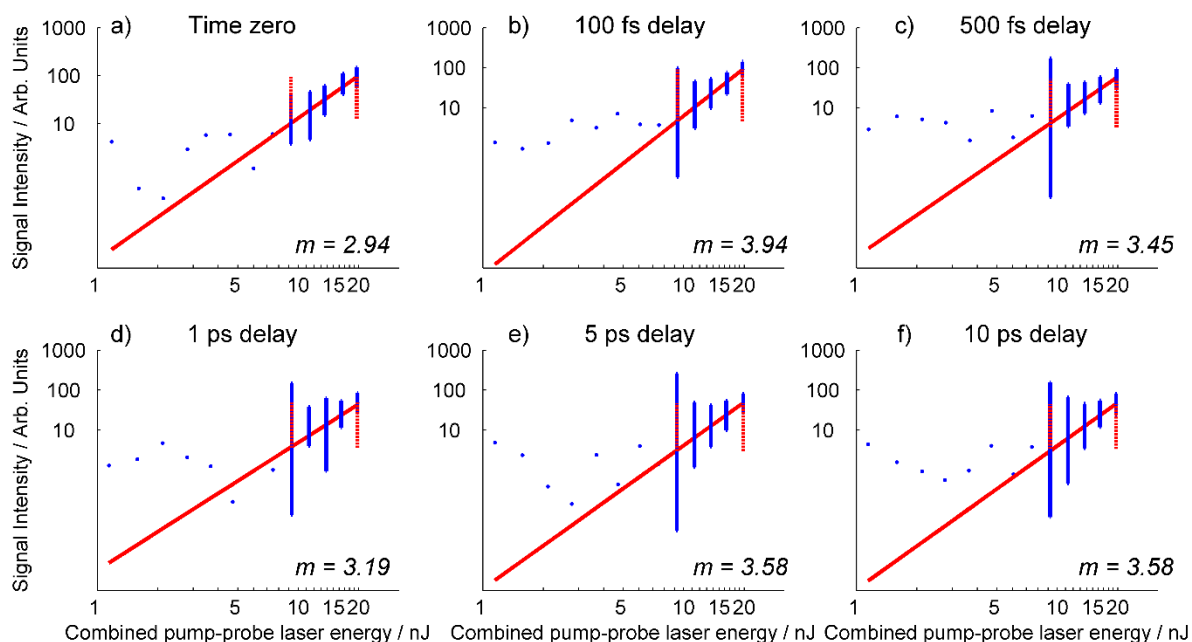


Figure S1: Power series for the 28 amu fragment ion.

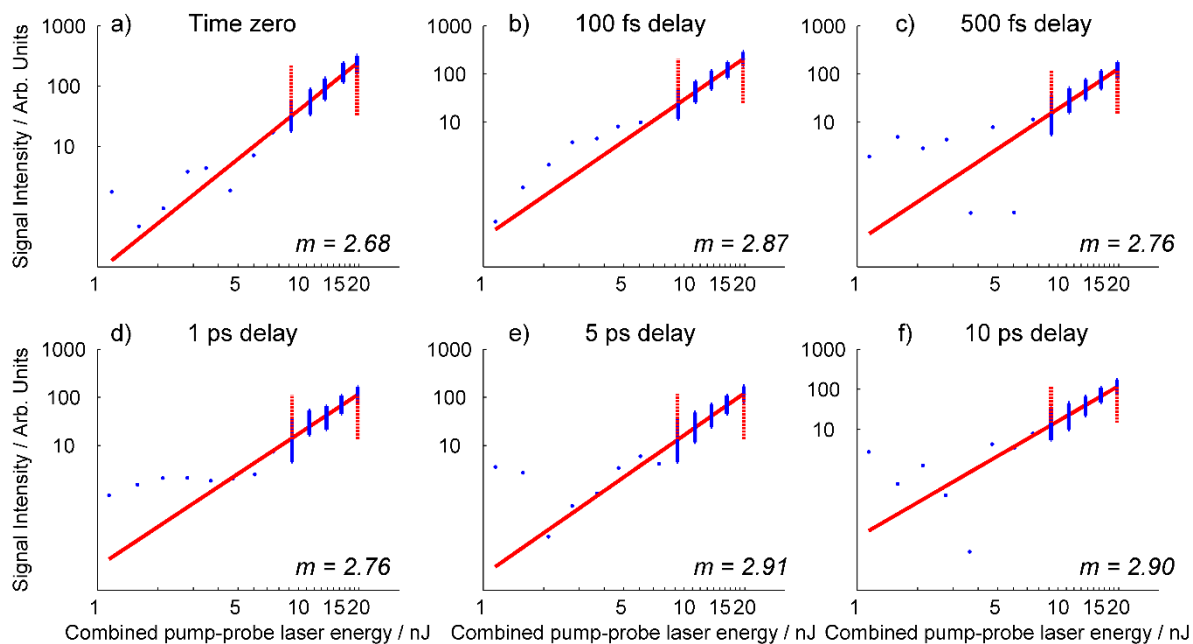


Figure S2: Power series for the 41 amu fragment ion.

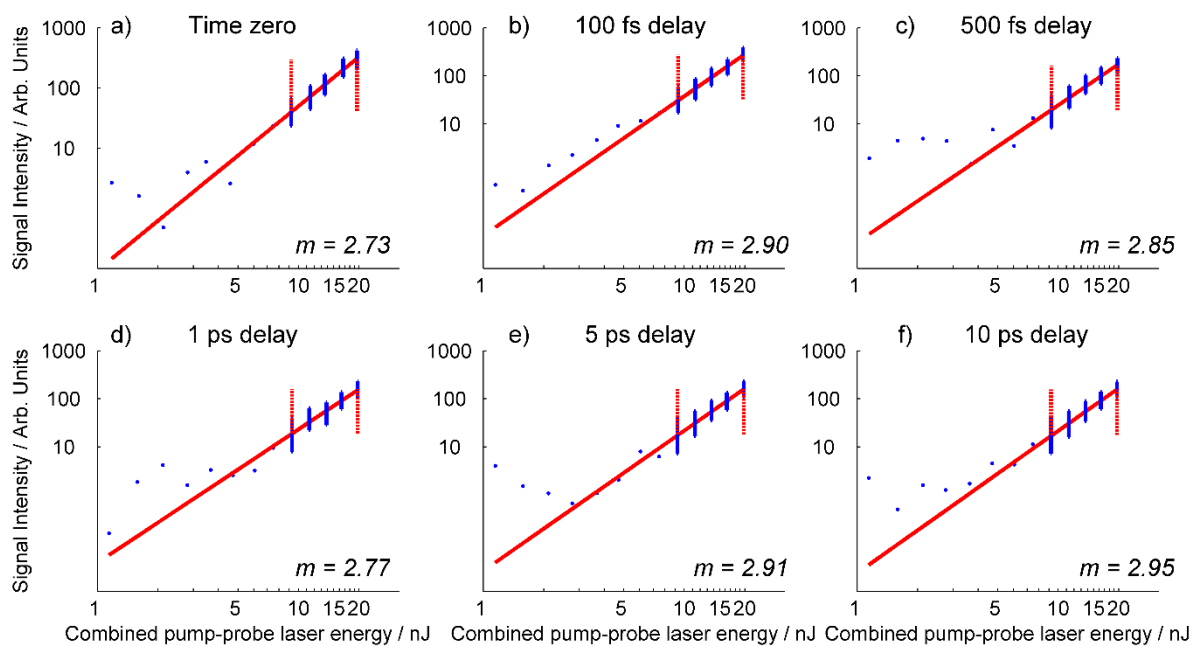


Figure S3: Power series for the 42 amu fragment ion.

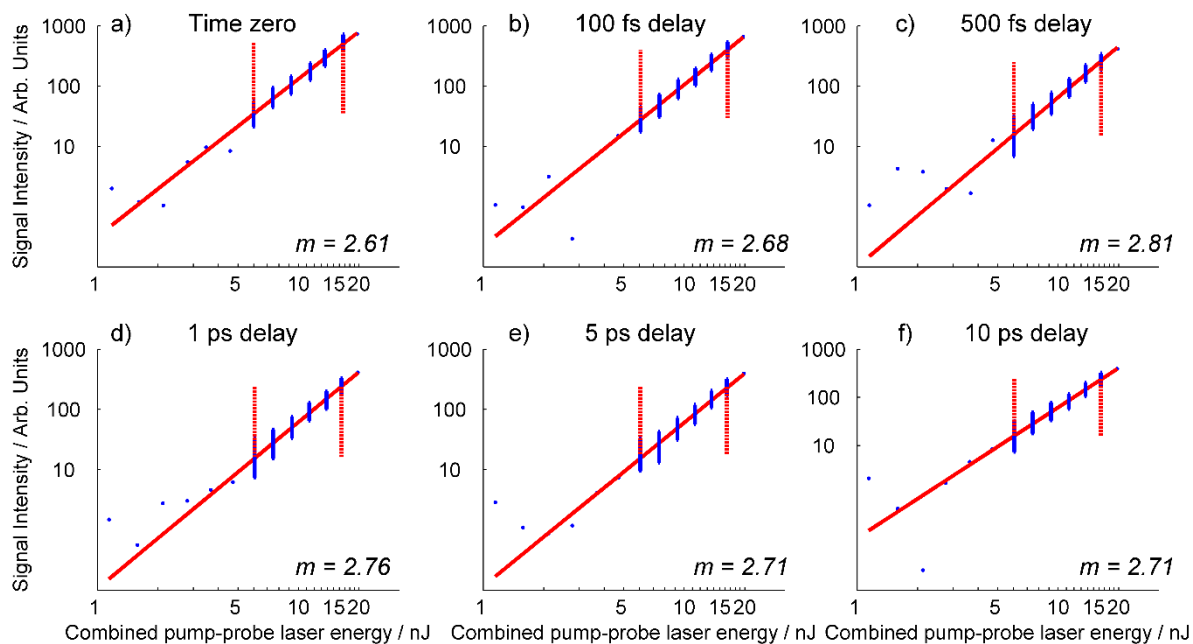


Figure S4: Power series for the 69 amu fragment ion.

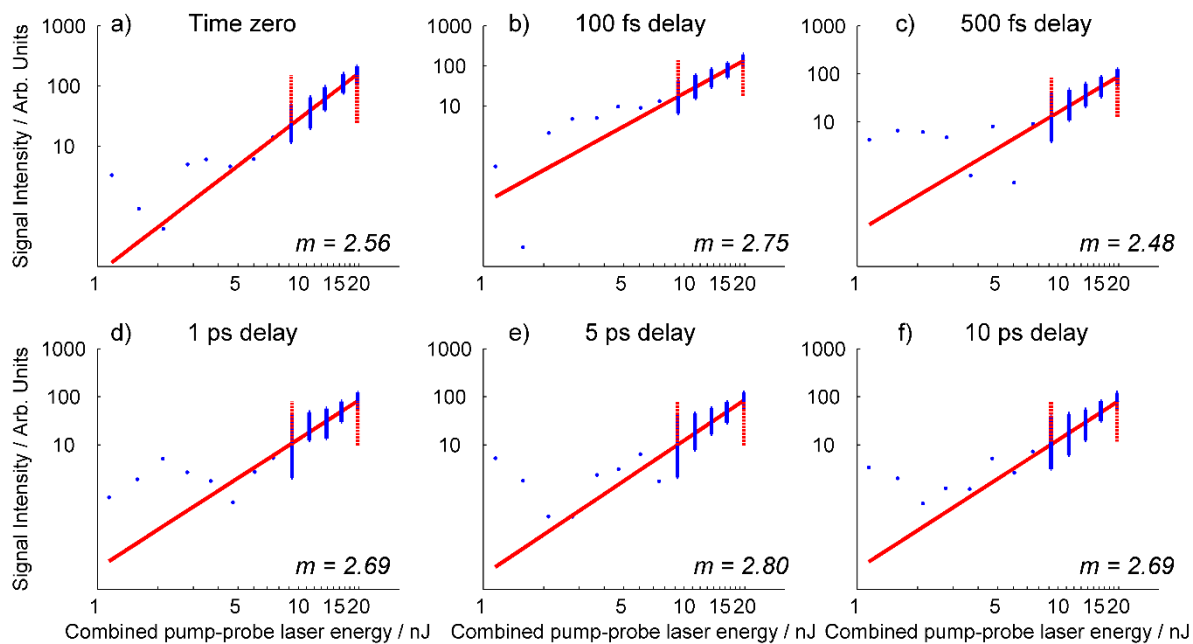


Figure S5: Power series for the 95 amu fragment ion.

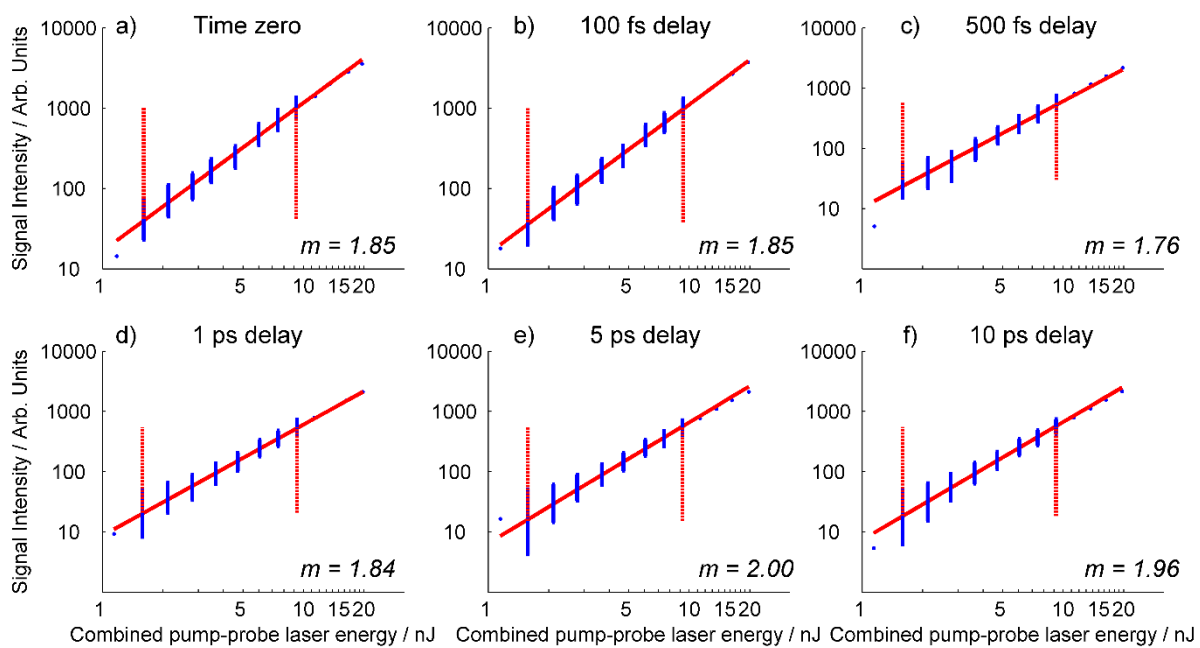


Figure S6: Power series for the parent (128 amu) ion.



## 2. Time-dependent UV/UV signal from pump-probe beams with equal power

The following relates to results discussed in Subsection 2.4. of the main paper. In Figures S7-S9, we present the remaining time-resolved signals for the 41, 42 and 95 amu fragment ions. The original data is represented by the blue dots, the fit of this data by the red line, and the background signal by the blue line. Inserts show the respective signal for the fragment ions extending out to 100 ps. It should be noted that for the 95 amu (Figure S9), a dip in the signal below the background level in the main plot between -0.75 and 1.5 ps is observed, but not for the longer scan seen in the insert performed between 0 and 100 ps. Despite both scans using the same laser power, this dip is likely caused by a saturation of the weak 95 amu signal, possibly due to slight focusing differences caused by laser-alignment checks performed between the two scans. Whilst unfortunate, we do not believe that this saturation affects the results significantly, as the decays observed for the 95 amu is similar to the other fragments.

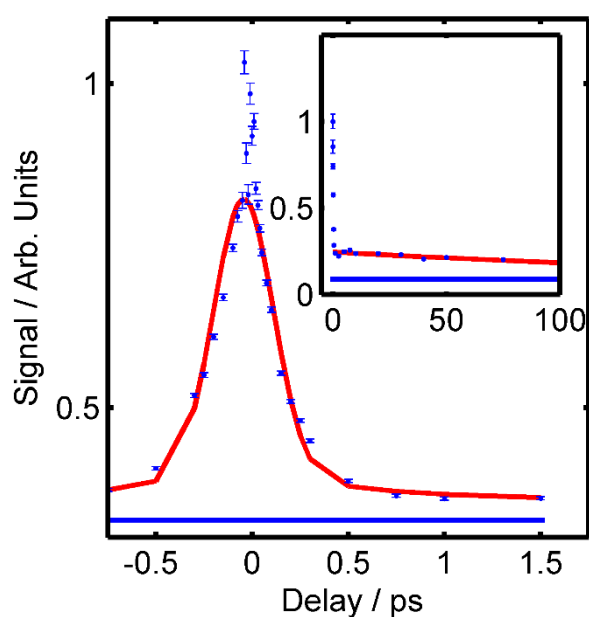


Figure S7: Time-dependent decay of the 41 amu fragment ion.

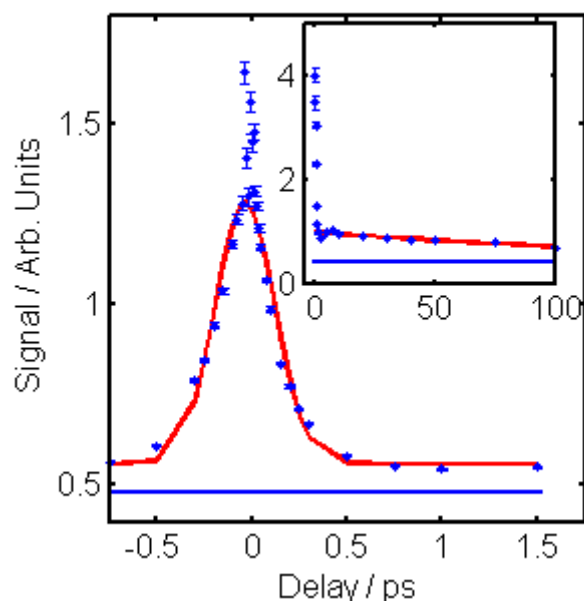


Figure S8: Time-dependent decay of the 42 amu fragment ion.

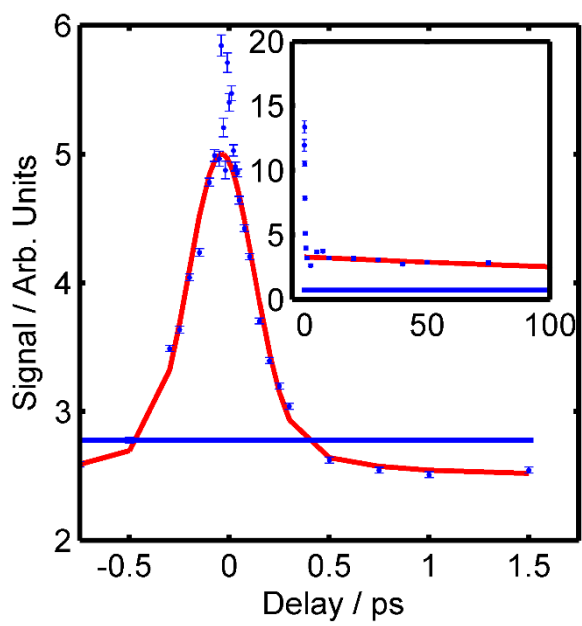


Figure S9: Time-dependent decay of the 95 amu fragment ion.

### 3. Time-dependent UV/UV signals from pump and probe beam with unequal powers

The following relates to results discussed in Subsection 2.5. of the main paper. In Figures S10-S13 we present the time-dependent signals observed for the 28, 41, 42 and 95 amu fragment ions when unequal pump and probe powers are used. In the images below, 3 nJ was used in the probe pulse, whilst 6 and 9 nJ per pulse was used in the pump beam. Experiments with 1.5 and 3 nJ per pulse in the pump beam were also performed, however, no significant signal above the background was observed for these fragments, and hence not presented. In each image, two plots are shown which dictate whether the pump pulse arrives first (pump-probe, blue) or if the probe pulse arrives first (probe-pump, red).

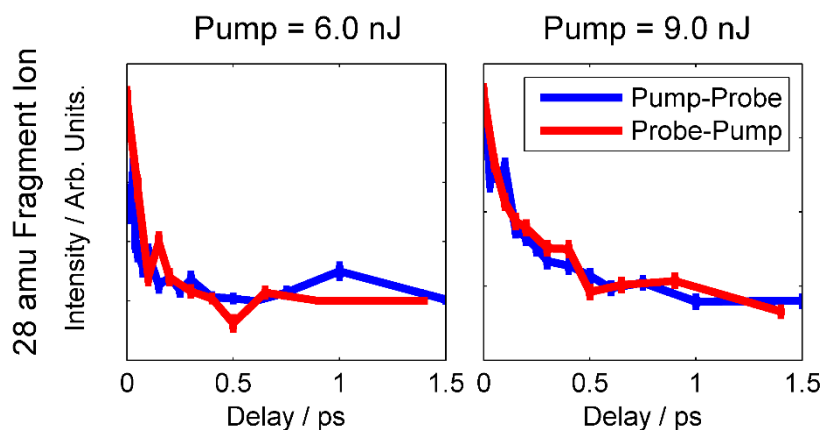


Figure S10: Inhomogeneous pump-probe signal for the 28 amu fragment ion.

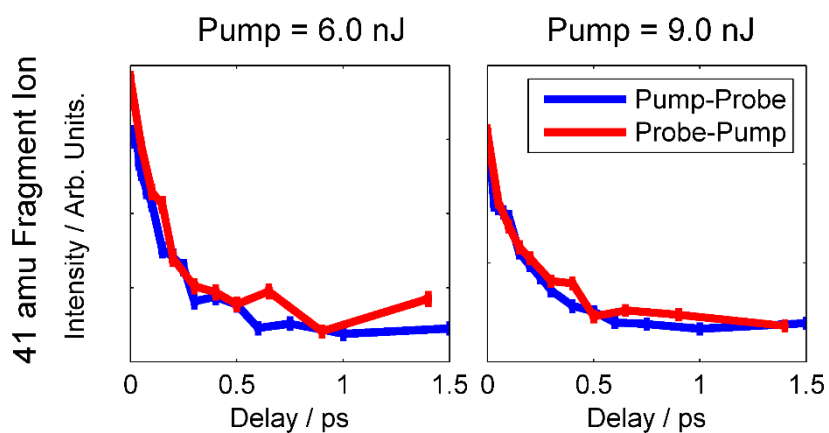


Figure S11: Inhomogeneous pump-probe signal for the 41 amu fragment ion.

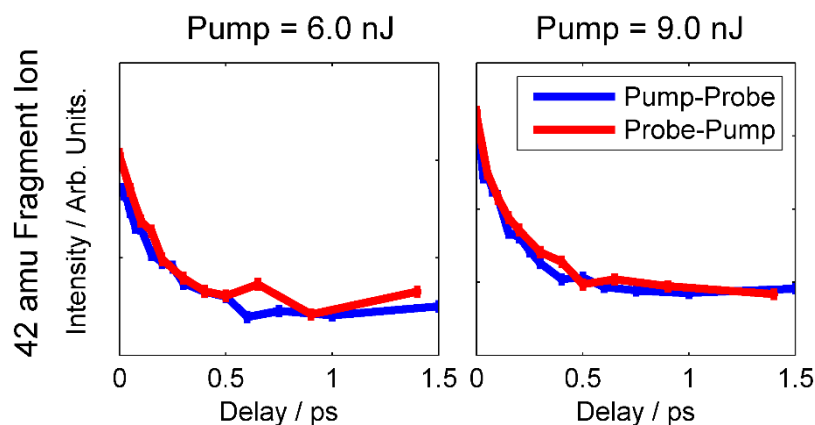


Figure S12: Inhomogeneous pump-probe signal for the 42 amu fragment ion.

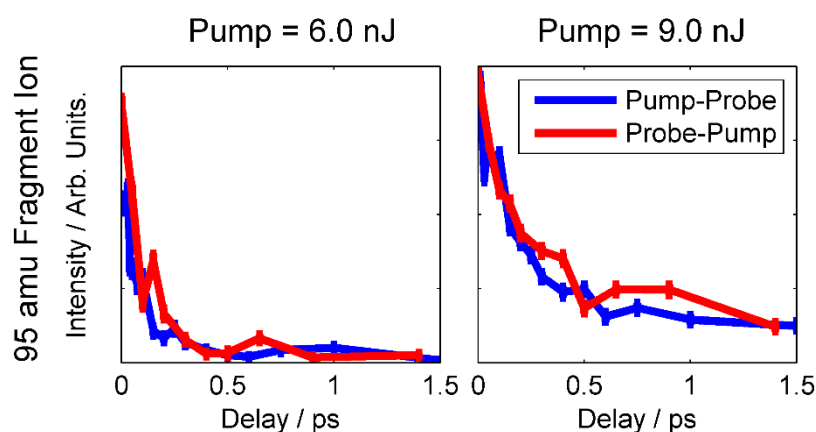


Figure S13: Inhomogeneous pump-probe signal for the 95 amu fragment ion

#### 4. Novelities of the 100 amu fragment

Due to its weak pump-probe signal, we did not explicitly discuss the 100 amu fragment ion in the main article. However, its appearance in the first place, especially in comparison to studies on uracil, is interesting, sparking questions as to how the fragment ion is formed, and what chemical formula can be attributed to it.

To produce the 100 amu fragment ion a 28 amu fragment must be lost from the parent 2-TU molecule. This is the first point of interest. When making comparisons to uracil, a loss of 28 amu from uracil would result in an 84 amu fragment ion. However, to our knowledge, the 84 amu fragment ion from uracil has not been observed in any single-photon ionisation or particle impact study [1–6]. This is in stark contrast to the results presented in Subsection 2.2., where the 100 amu fragment ion of 2-TU appears in the single-photon VUV experiments.

Whilst not observable in single-photon experiments, Eden *et al.* have demonstrated that the 84 amu fragment ion of uracil can be observed in select multi-photon ionization experiments using nanosecond pulses at a wavelength of  $\leq 232$  nm (i.e.  $\geq 5.34$  eV) [7–9]. Femtosecond pump-probe studies with a delay of up to 100 ps between the two pulses failed to produce the fragment, leaving them to suggest that the fragment is created through a long-lived excited state in uracil after dynamics are initially launched on the  $S_3$  rather than  $S_2$  state [8]. With the use of high-resolution mass spectra of both uracil and deuterated uracil, Eden *et al.* were able to attribute the 84 amu fragment ion to  $C_3H_4N_2O^+$ , ultimately suggesting

that the loss of the 28 amu was due to a CO ejection after a ring-opening process involving through the N<sub>3</sub>-C<sub>4</sub> bond [7–9].

Due to the same mass loss, it is possible that the 100 amu fragment ion of 2-TU is also created through the ejection of CO, leaving behind C<sub>3</sub>H<sub>4</sub>N<sub>2</sub>S, which is then ionized by the probe pulse. It is also possible, due its appearance in the multi-photon UV/UV experiments, the 100 amu fragment ion of 2-TU is created through a similar type of ring-opening process that Eden *et al.* suggested for uracil, albeit on a much faster timescale. However, the appearance of the 100 amu fragment ion in the single-photon VUV experiment presented in Section 2.2. shows that the multi-photon route is not an exclusive one, unlike what has been seen so far for the 84 amu fragment ion of uracil. Additionally, the multi-photon appearance of the 100 amu fragment ion from 2-TU does not seem to be as wavelength selective as what is observed for the 84 amu fragment ion of uracil [7–9]. In a mass spectrum presented by Yu *et al.*, created through multi-photon probing using a 290 nm pump, the 100 amu fragment was still observed for 2-TU [10]. This excludes the idea that dynamics are being launched on states higher than the S<sub>2</sub>. However, it should be noted that in the mass spectra of 4-thiouracil and 2,4-dithiouracil by Hecht *et al.* both show peaks at 100 amu and 116 amu, respectively, which also indicate a loss of 28 amu from their respective parent structures [4]. As there is no oxygen atom on 2,4-dithiouracil, this may indicate that the 28 amu loss is instead something common to the three thionated uracil molecules (i.e. N<sub>2</sub> or HCNH rather than CO). Unfortunately, the results presented here do not allow us to draw conclusion to one model or another. Despite these uncertainties, this discussion here may ultimately show that the loss of the 28 amu fragment may prove crucial in investigating the subtle differences in the dynamics between the thiouracils and uracil.

## 5. References

1. Jochims, H.W.; Schwell, M.; Baumgärtel, H.; Leach, S. Photoion mass spectrometry of adenine, thymine and uracil in the 6–22 eV photon energy range. *Chem. Phys.* **2005**, *314*, 263–282, doi:10.1016/j.chemphys.2005.03.008.
2. Denifl, S.; Sonnweber, B.; Hanel, G.; Scheier, P. Threshold electron impact ionization studies of uracil. *Int. J. of Mass Spectrom.* **2004**, *238*, 47–53, doi:10.1016/j.ijms.2004.07.010.
3. Coupier, B.; Farizon, B.; Farizon, M.; Gaillard, M.J.; Gobet, F.; De Castro Faria, N. V.; Jalberty, G.; Ouaskit, S.; Carré, M.; Gstir, B.; et al. Inelastic interactions of protons and electrons with biologically relevant molecules. *Eur. Phys. J. D* **2002**, *20*, 459–468, doi:10.1140/epjd/e2002-00166-3.
4. Hecht, S.M.; Gupta, A.S.; Leonard, N.J. Position of uridine thiation: The identification of minor nucleosides from transfer RNA by mass spectrometry. *BBA Sect. Nucleic Acids Protein Synth.* **1969**, *182*, 444–448, doi:10.1016/0005-2787(69)90195-6.
5. Rice, J.M.; Dudek, G.O.; Barber, M. Mass Spectra of Nucleic Acid Derivatives. Pyrimidines. *J. Am. Chem. Soc.* **1965**, *87*, 4569–4576, doi:10.1021/ja00948a029.
6. Nelson, C.C.; McCloskey, J.A. Collision-induced dissociation of uracil and its derivatives. *J. Am. Soc. Mass Spectrom.* **1994**, *5*, 339–349, doi:10.1016/1044-0305(94)85049-6.
7. Barc, B.; Ryszka, M.; Spurrell, J.; Dampc, M.; Limão-Vieira, P.; Parajuli, R.; Mason, N.J.; Eden, S. Multi-photon ionization and fragmentation of uracil: Neutral excited-state ring opening and hydration effects. *J. Chem. Phys.* **2013**, *139*, doi:10.1063/1.4851476.
8. Ghafur, O.; Crane, S.W.; Ryszka, M.; Bockova, J.; Rebelo, A.; Saalbach, L.; De Camillis, S.; Greenwood, J.B.; Eden, S.; Townsend, D. Ultraviolet relaxation dynamics in uracil: Time-resolved photoion yield studies using a laser-based thermal desorption source. *J. Chem. Phys.* **2018**, *149*, 034301,

doi:10.1063/1.5034419.

9. Ryszka, M.; Pandey, R.; Rizk, C.; Tabet, J.; Barc, B.; Dampc, M.; Mason, N.J.; Eden, S. Dissociative multi-photon ionization of isolated uracil and uracil-adenine complexes. *Int. J. Mass Spectrom.* **2016**, *396*, 48–54, doi:10.1016/j.ijms.2015.12.006.
10. Yu, H.; Sanchez-Rodriguez, J.A.; Pollum, M.; Crespo-Hernández, C.E.; Mai, S.; Marquetand, P.; González, L.; Ullrich, S. Internal conversion and intersystem crossing pathways in UV excited, isolated uracils and their implications in prebiotic chemistry. *Phys. Chem. Chem. Phys.* **2016**, *18*, 20168–20176, doi:10.1039/c6cp01790h.